Effective Synthesis of Iron-Carbonyl Small Rings and Macrocycles *via* Migratory Insertion Reactions

by

Aaron Leung

A thesis

Presented to the University of Waterloo

in fulfillment of the

thesis requirement for the degree of

Master of Science

In

Chemistry

Waterloo, Ontario, Canada, 2019

Author's Declaration

I hereby declare that I am the sole author of this thesis. This is a true copy of the thesis, including any required final revisions, as accepted by my examiners. I understand that my thesis may be made electronically available to the public.

Abstract

Migratory insertion reactions (MIRs) of ^{P}FpR [^{P}Fp = $(PPh_2(CH_2)_3Cp)Fe(CO)_2$, R = $(CH_2)_5CH_3$ or $(CH_2)_4CH{=}CH_2$], which involve migratory insertion polymerization (MIP) and intramolecular migratory insertion cyclization (MIC), produce P(^{P}FpR) macrocycles and cyclized ^{P}FpR rings, respectively. MIC occurred at the early stage of MIR, while MIP exclusively underwent ring-closing with no linear analogues generated. The effect of solvent, temperature and the concentration of ^{P}FpR on MIR was investigated, based on which the competition of MIP and MIC was regulated for the effective synthesis of P(^{P}FpR) or cyclized ^{P}FpR rings. Cyclized ^{P}FpR was synthesized as the only product in THF with a low concentration of ^{P}FpR (1 wt. %), while ring-closing MIP was predominated under the condition at 60 °C with high monomer concentration of ^{P}FpR in THF (> 70 wt. %) resulting in P(^{P}FpR) macrocycles with M_n up to 17,500 g/mol. This effective synthesis of ring molecules is attributed to the piano-stool coordination geometry and the low rotation barrier of Cp-Fe bond, and will facilitate further exploration of ring molecules as functional materials and supramolecular building blocks.

Acknowledgement

First of all, I would like to express my most sincere gratitude to my supervisor, Dr. Xiaosong Wang, for giving me this research opportunity as a Master student in his research group, as well as his patience and guidance in the past two years. He has encouraged me to be confident in myself and has given me many opportunities to develop new practical skills. I would also like to sincerely thank my committee members (Dr. Jean Duhamel and Dr. Mario Gauthier) for providing useful advice and suggestions on my research work.

Next, I would like to thank Janet Venne, Janine Thoma, Val Goodfellow, Dr. Richard Smith, and Dr. Jalil Assoud for their technical support on the NMR, GPC, MS, and crystallography instrumentation. I would also like to thank Catherine Van Each for her kind help during my Master's studies at the University of Waterloo to ensure I can graduate on time.

I would also like to thank all my amazing lab mates, including Dr. Dapeng Liu, Dr. Peng Liao, Diya Geng, Yang Yang, Dr. Nicholas Lanigan, Li Zhao, Dr. Huiwen He, Yuanting Cai, Jing Kang, Weicheng Peng, Jyunhao Sie, Dr. Weiwei Cheng for always being supportive and kind to me.

Last but not least, I would like to show my greatest appreciation to my family and friends for their continuous love, patience, and understanding. Their support and encouragement have motivated me to complete this Master's program.

I truly appreciate everyone whom I have met along this exciting journey, for being a part of it and making it a memorable one. Thank you!

Dedication

This thesis is dedicated to my beloved parents and sister, who have shown their unconditional love and support since the very first day of this journey. This journey would not have been possible without them.

Table of Contents

Author's declaration ii

Abstract iii

Acknowledgement iv

Dedication v

List of Figures ix

List of Schemes xi

List of Tables xii

List of Abbreviations xiii

1.0 Introduction 1

1.1 Organometallic Ring Complexes 1

1.1.1 Metal-Carbonyl Ring Complexes 2

1.1.2 Cp-Phosphane Ligand Complexes 5

1.2 Introduction to Cyclic Polymers 7

1.2.1 Synthetic Routes for Cyclic Polymers 10

1.2.2 Metal-Containing Cyclic Oligomers 11

1.2.3 Metal-Containing Cyclic Polymers 13

1.2.4 Characterization Methods 14

1.2.4.1 Gel Permeation Chromatography 14

1.2.4.2 End Group Analysis 15

1.2.4.3 Atomic Force Microscopy 17

1.2.4.4 Transmission Electron Microscopy 18

1.3 Migratory Insertion Reaction 19

1.3.1 MIP of FpP 20

1.3.2 MIP of ^{P}FpR 22

2.0 Experimental 24

2.1 Materials and Instrumentations 24

2.2 Synthesis of P(FpP) 25

2.2.1 Synthesis of FpK 25

2.2.2 Synthesis of PPh_2Na 26

2.2.3 Synthesis of $Ph_2P(CH_2)_3Cl$ 26

2.2.4 Synthesis of FpP 27

2.2.5 Synthesis of P(FpP) 28

2.3 Synthesis of ^{P}FpR 28

2.3.1 Synthesis of FpR 29

2.3.2 Synthesis of ^{Cl}FpR 29

2.3.3 Synthesis of ^{P}FpR 30

2.4 Synthesis of P(^{P}FpR) Macrocycles 31

2.5 Synthesis of Cyclic ^{P}FpR Small Rings 32

3.0 Results and Discussion 34

3.1 P(^{P}FpR) Macrocycles Characterization 36

3.1.1 End Group Analysis by NMR 36

3.1.2. Cyclic Topology by TEM Analysis 37

3.1.3 Molecular Weight by MALDI-TOF Analysis 38

3.1.4 Molecular Weight by GPC Analysis 40

3.2 Fe-P Bonded ^{P}FpR Rings Characterization 41

3.2.1 X-ray Crystallography 41

3.2.2 NMR Characterization 44

3.2.3 Other Characterizations 49

3.3 Polymerization Condition Effects on MIR 50

3.3.1 Solvent and Temperature Effects on MIP 50

3.3.2 Kinetic Study on Ring-closing MIP of ^{P}FpR 52

3.3.3 Concentration Effect on MIP 53

4.0 Conclusions 56

5.0 Future Work 57

References 58

Appendix 61

A1. NMR Characterization of Cyclic ^{P}FpR Ring, for R = $(CH_2)_5CH_3$ 61

List of Figures

Figure 1.1: A general illustration of organometallic ring complexes. 1

Figure 1.2: Bonding interactions of MC complexes. 3

Figure 1.3: Illustration of a MC ring complex bearing a Cp-P bidentate ligand. 5

Figure 1.4: Ionic radius of alkali metal cations and the diameter of crown ether cavity. 8

Figure 1.5: The X-ray crystal structure of ferrocene ring. 13

Figure 1.6: GPC traces of linear $PBNP_{20}$-(b-$PTNP_{20})_2$ and cyclic $PBNP_{10}$-(b-$PTNP_{20})_2$-b-$PBNP_{10}$. 15

Figure 1.7: Overlay MALDI-TOF spectra for linear and cyclic PFS. 16

Figure 1.8: AFM images for PCEVE-PS cyclic polymer brushes. 17

Figure 1.9: AFM analysis for c-[$PBNP_{10}$-(b-$PTNP_{160})_2$-b-$PBNP_{10}$]-POSS. 18

Figure 1.10: TEM images c-[$PBNP_{10}$-(b-$PTNP_{160})_2$-b-$PBNP_{10}$]-POSS. 19

Figure 1.11: Reactions of FpP. 21

Figure 1.12: The ^{31}P NMR spectrum for P(FpP). 22

Figure 1.13: TEM, AFM images, and ^{31}P NMR spectrum for P(^{P}FpR) macrocycles. 23

Figure 3.1: ^{31}P NMR spectra for the crude and separated products. 35

Figure 3.2: ^{1}H NMR spectra for the crude and separated products. 35

Figure 3.3: End group analysis of linear P(FpP) and cyclic P(^{P}FpR) polymers. 37

Figure 3.4: TEM image for P(^{P}FpR) macrocycles. 38

Figure 3.5: GPC elution curve for P(^{P}FpR) macrocycles. 41

Figure 3.6: ORTEP drawings for the molecular structures of cyclic ^{P}FpR 42

Figure 3.7: ^{1}H NMR spectrum for cyclic ^{P}FpR, for R = $(CH_2)_4CH{=}CH_2$. 44

Figure 3.8: ^{13}C NMR spectrum for cyclic ^{P}FpR, for R = $(CH_2)_4CH=CH_2$. 45

Figure 3.9: COSY 2D NMR spectrum for cyclic ^{P}FpR, for R = $(CH_2)_4CH=CH_2$. 47

Figure 3.10: HMQC 2D NMR spectrum for cyclic ^{P}FpR, for R = $(CH_2)_4CH=CH_2$. 48

Figure 3.11: FT-IR spectra for cyclic ^{P}FpR 49

Figure 3.12: ESI-MS spectra for cyclic ^{P}FpR. 50

Figure 3.13: ^{31}P NMR spectra for crude products in via MIP in different solvents. 52

Figure 3.14: Time-dependent ^{31}P NMR spectra for the MIP of ^{P}FpR. 53

Figure 3.15: ^{31}P NMR spectra for P(^{P}FpR) at different concentrations. 54

Figure 3.16: GPC data for P(^{P}FpR) at different concentrations. 55

Figure 4.1: Summary of MIRs of ^{P}FpR. 56

Figure A1: ^{1}H NMR spectra for cyclic ^{P}FpR. 62

Figure A2: ^{13}C NMR spectra for cyclic ^{P}FpR 62

Figure A3: COSY NMR spectra for cyclic ^{P}FpR 63

Figure A4: HMQC NMR spectra for cyclic ^{P}FpR. 64

List of Schemes

Scheme 1.1: A general scheme for ROP of metallocenophanes. 2

Scheme 1.2: Reactions of MC complexes. 3

Scheme 1.3: Synthesis and ROP of a Si-C bridged MC ring complex. 4

Scheme 1.4: Transmetallation of Cp-phosphane ligands. 6

Scheme 1.5: Synthesis and applications of a manganese-carbonyl ring complex. 7

Scheme 1.6: Synthesis of cyclic brush polymer by REMP and a "grafting from" technique. 9

Scheme 1.7: ROMP of 1,5-cyclooctadiene. 10

Scheme 1.8: Ring-closing polymerization of a linear PS chain 11

Scheme 1.9: Synthesis of polyvinylferrocene *via* radical polymerization. 12

Scheme 1.10: Synthesis of cyclic PFS *via* intramolecular backbiting reaction. 14

Scheme 1.11: General scheme for MIR *via* CO insertion. 20

Scheme 1.12: Synthesis and MIP of FpP. 21

Scheme 1.13: Synthetic scheme and MIP of ^{P}FpR. 23

Scheme 2.1: Synthesis of P(FpP). 25

Scheme 2.2: Synthesis of FpK 26

Scheme 2.3: Synthesis of PPh_2Na. 26

Scheme 2.4: Synthesis of $Ph_2P(CH_2)_3Cl$. 27

Scheme 2.5: Synthesis of FpP. 27

Scheme 2.6: Synthetic scheme for the preparation of ^{P}FpR. 28

Scheme 3.1: Intramolecular MIC of ^{P}FpR. 42

Scheme 5.1: Post-polymerization modification of P(^{P}FpR) macrocycles by click reactions. ... 57

List of Tables

Table 3.1: MALDI-TOF experiments with different matrices 39

Table 3.2: Summary of crystallographic data for cyclic ^{P}FpR 43

Table 3.3: Elemental analysis results for cyclic ^{P}FpR 49

List of Abbreviations

ACN	Acetonitrile
AFM	Atomic force microscopy
^{Cl}FpR	$(Cl(CH_2)_3Cp)Fe(CO)_2R$
COSY	Correlation spectroscopy
Cp	Cyclopentadienyl
DCM	Dichloromethane
DMF	Dimethylformamide
DMSO	Dimethylsulfoxide
DP	Degree of polymerization
eq	Molar equivalent
ESI	Electrospray ionization
Fp_2	Cyclopentadienyl dicarbonyl iron dimer
FpK	Cyclopentadienyl dicarbonyl iron potassium
FpP	$CpFe(CO)_2[(CH_2)_3PPh_2]]$
FpR	$CpFe(CO)_2R$
FT-IR	Fourier-transform infrared spectroscopy
GPC	Gel permeation chromatography
HMQC	Heteronuclear multiple quantum coherence
IR	Infrared spectroscopy
M_p	Peak molecular weight
MALDI-TOF	Matrix assisted laser desorption ionization- time of flight

MC	Metal-carbonyl
MIC	Migratory insertion cyclization
MIP	Migration insertion polymerization
MIR	Migratory insertion reaction
MS	Mass spectroscopy
MW	Molecular weight
NMR	Nuclear magnetic resonance
PDI	Polydispersity index
P(FpP)	Poly(cyclopentadienyl carbonyl diphenylphosphinobutanoyl iron)
P(^{P}FpR)	Poly[$(PPh_2(CH_2)_3Cp)Fe(CO)_2R$]
^{P}FpR	$(PPh_2(CH_2)_3Cp)Fe(CO)_2R$
PFS	Poly(ferrocenylsilane)
PS	Polystyrene
RB	Round bottom
RCM	Ring-closing metathesis
REMP	Ring expansion metathesis polymerization
ROP	Ring opening polymerization
ROMP	Ring opening metathesis polymerization
TEM	Transmission electron microscopy
TFA	Trifluoroacetic acid
THF	Tetrahydrofuran

1.0 Introduction

1.1 Organometallic Ring Complexes

Organometallic rings are cyclic complexes that contain transition metal atoms and organic ligands. They usually consist of a bidentate ligand, in which the two ligands (homobidentate or heterobidentate) are connected by a linker and coordinated to the same metal centre to form the ring (Figure 1.1a), such as bridged metallocenes (Figure 1.1b) and metal-carbonyl (MC) ring complexes (Figure 1.1c). Over the past 50 years, a significant amount of research on organometallic ring complexes has been completed, and complexes with numerous combinations of transition metals and ligands have also been reported. Tremendous effort has also been made in exploring their applications, and some of them were found to show promising applications as monomers in ring opening polymerization (ROP)[1] and as catalysts in asymmetric reactions[2-4]. Although extensive research has already been done in the field, improvement on synthetic reactions and their applications, as well as the continuous development of novel organometallic rings are necessary and should always be considered.

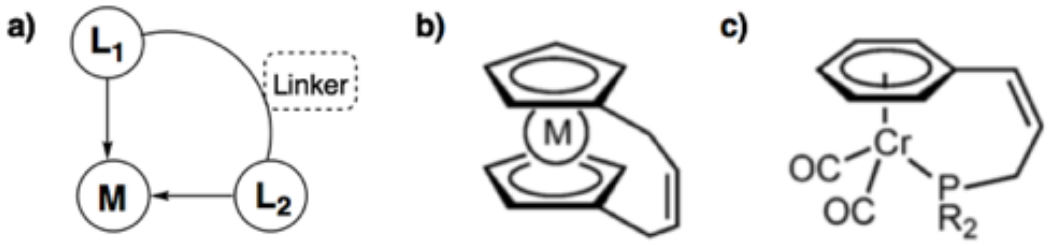

Figure 1.1: a) A general illustration of organometal ring complexes bearing a bidentate ligand; b) bridged metallocenes; and c) chromium-carbonyl ring complex, where M = transition metal, L = ligands.[3]

For example, Manners *et al.* reported ROP using strained metallocenophanes as monomers, which contain homobidentate cyclopentadienyl (Cp) ligands that are usually linked by a short (1-

3 atoms) spacer group (Scheme 1.1). These strained metallocenophanes have exhibited unusual reactivity due to the high ring-strained environment, and they were found to undergo ROP effectively to form high molecular weight (MW) polymers.[5] The applications of strained metallocenophanes in ROP has led to rapid growth in the advanced development of metallocenophanes as monomers with different metal centres (*i.e*. Fe, Co, Zr, Mo, Ru, Cr, etc.), spacer groups (*i.e*. C, Si, P, As, S, Se, etc.), and substituents on Cp ligands for ROP. These combinations were believed to provide some unique properties with important applications of the resulting polymers.[5,6]

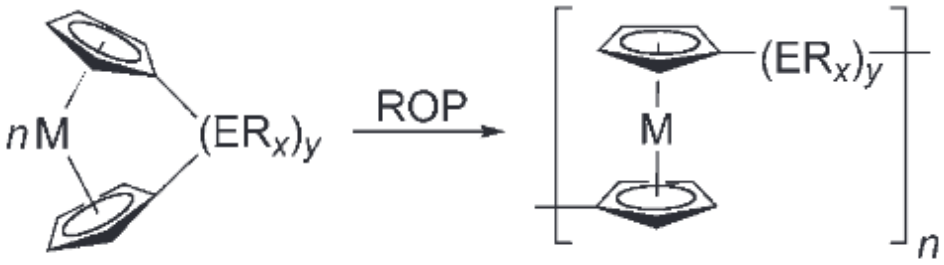

Scheme 1.1: A general scheme for ROP of metallocenophanes, where M = transition metal, E = main group element, and R = substituents.[6]

1.1.1 Metal-Carbonyl (MC) Ring Complexes

MC complexes are considered as one of the commonly used systems in organometallic chemistry. They involve the coordination of a carbon monoxide (CO) ligand to a transition metal center, forming a metal-carbon (M-C) coordination bond. They can either be coordinated as a terminal CO ligand or as a bridging CO ligand between two or more metal atoms. CO ligands can serve as a σ-donor and a π-acceptor ligand, without affecting the oxidation state of the binding metals. MC systems involve two types of bonding interactions. They are ligand-to-metal sigma (σ) bonding interactions and metal-to-ligand pi (π) backbonding interactions. In such a system, σ bonds are formed when the empty orbitals of the metal center accept electrons from the CO ligands

(Figure 1.2a), whereas π bonds are formed when the d-orbitals of the metal 'back-donate' its electrons to the empty anti-bonding orbitals of the CO ligands (Figure 1.2b).[7] These sigma and pi bonding interactions can strengthen the M-C bonds and enhance the overall stability of the MC complexes. Moreover, due to its unusual reactivity, MC complexes commonly serve as starting materials in organometallic synthesis, such as ligand substitution *via* CO release (Scheme 1.2a) and 1,1-insertion reaction (Scheme 1.2b), to form other useful derivatives for functional materials.[8,9]

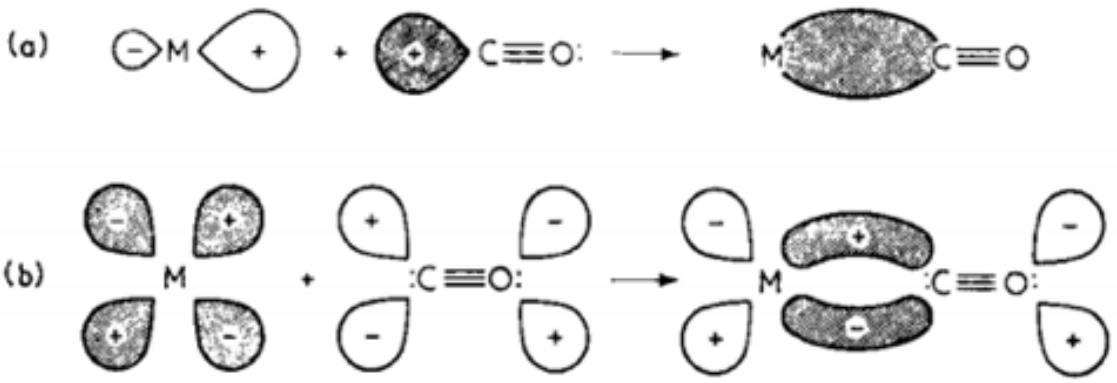

Figure 1.2: Bonding interactions of MC complexes. a) Formation of sigma bond via electron donation from the carbonyl ligand; b) formation of pi bond via back-bonding of the metal.[7]

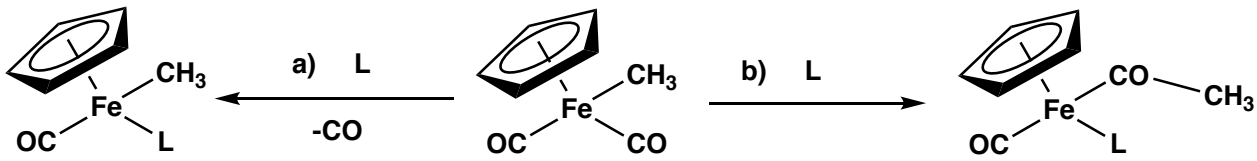

Scheme 1.2: Reactions of MC complexes. a) ligand substitution and b) 1,1-insertion of $CpFe(CO)_2CH_3$

MC ring complexes usually contain heterobidentate ligands. Their properties and applications can therefore be very different depending on the nature of the ligands. Pannell *et al.* demonstrated the synthesis and ROP of a Si-C-bridged MC ring complex, (η^5-C_5H_4-

Si)Fe(CO)$_2$(CH$_2$SiR$_2$) (3 in Scheme 1.3).[10] The ring formation was achieved by an intramolecular salt-elimination reaction of (η^5-C$_5$H$_4$)Fe(CO)$_2$(SiR$_2$CH$_2$Cl) (1 in Scheme 1.3) or (η^5-C$_5$H$_4$)Fe(CO)$_2$(CH$_2$SiR$_2$Cl) (2 in Scheme 1.3) upon metalation of the Cp with lithium diisopropylamide (LDA) as a strong base. The silyl group in 1 migrated to the Cp anion during the reaction, producing iron anions and the Li counter-cations for ring-closing salt elimination reaction, whereas 2 simply underwent intramolecular salt elimination between Cl and the Li counter-cations on the Cp to form the ring.[10] The resulting polymer (4 in scheme 1.3) was obtained in quantitative yield upon solvent evaporation of 3, producing a new class of MC polymers with a relatively high MW of *ca*. 72,000 g/mol for 4a. These resulting polymers are stable in the atmosphere, and films can be cast from THF solutions over time as a result of polymer cross-linking.[10]

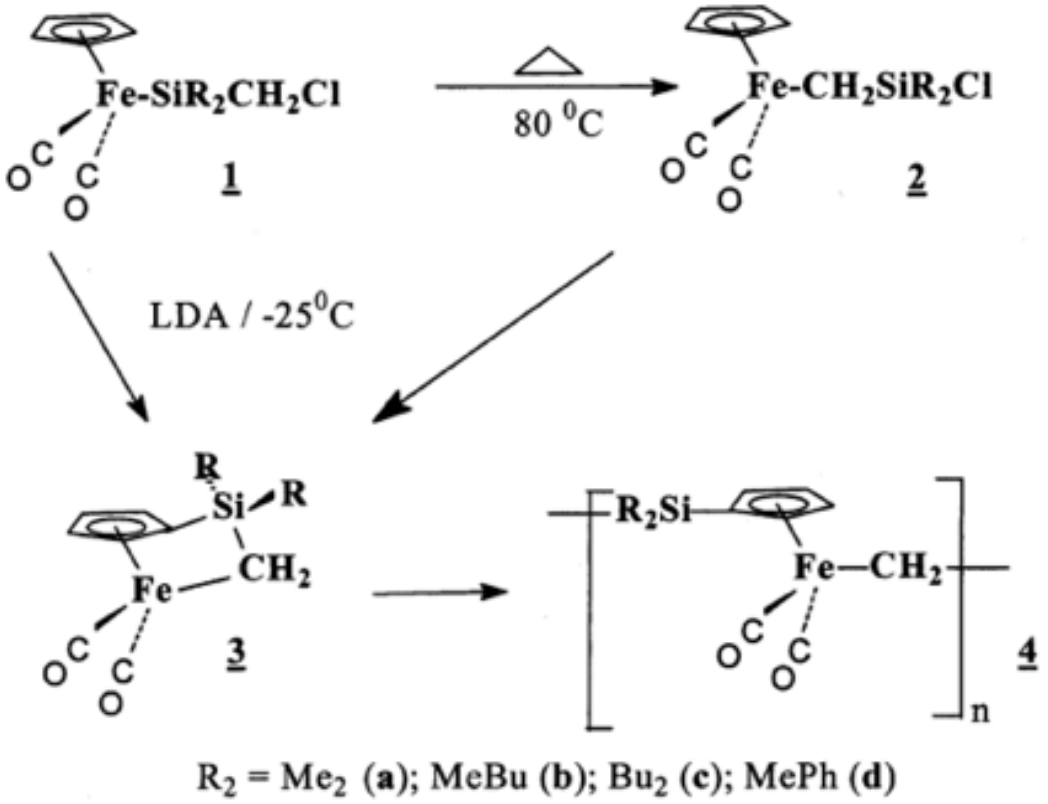

Scheme 1.3: Synthesis and ROP of a Si-C bridged MC ring complex, 3.[10]

1.1.2 MC Ring Complexes with Cp-Phosphane Ligands.

Cp and phosphine ligands (Figure 1.2) are among the most commonly used ligands in organometallic chemistry, due to their very different properties in nature. The Cp moiety is a negatively charged π ligand, whereas the phosphane moiety is an electroneutral nucleophilic ligand. The Cp-phosphane heterobidentate ligands have therefore been extensively studied and proven to provide new insights on chirality and their applications in asymmetric catalysis.[2,3,4] MC ring complexes containing Cp-phosphane bidentate ligands are commonly prepared by metal-ligand coordination (transmetallation), in which the bidentate ligands are first prepared prior to metal coordination.

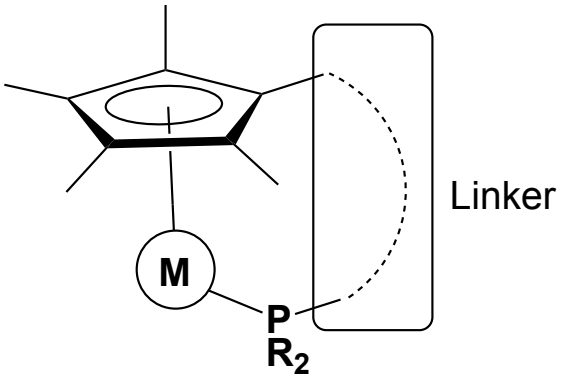

Figure 1.3: Illustration of a MC ring complex bearing a Cp-phosphane bidentate ligand, separated by a linker.

For example, Cole-Hamilton and coworkers reported the synthesis of group 9 MC ring complexes by metal-ligand coordination (Scheme 1.4).[11] A bidentate ligand containing the Cp and phosphane moieties were first synthesized *via* a 4-step reaction. 1,2,3,4-Tetramethylcyclopentadiene was used as the starting material, followed by metalation with the addition of butyllithium as the strong base. An ethyl chloride spacer was then added to the Cp moiety by a salt elimination reaction, followed by substitution of the Cl atom with the phosphane group. After the synthesis of the bidentate ligand, group 9 MC complexes, including $Co_2(CO)_8$,

$[RhCl(CO)_2]_2$, and $[IrCl(CO)(PPh_3)_2]$, were added for the subsequent metal-ligand coordination (Scheme 1.4). Ring formation was confirmed by ^{1}H, ^{13}C and ^{31}P nuclear magnetic resonance (NMR) spectroscopies and x-ray crystallography.[11] Other ring complexes containing Cp-phosphane bidentate ligands with various early and late transition metals, including Co,[12] Cr,[13], Ti,[14] Zr,[15] Ni,[16] and Mn,[16] have also been synthesized using metal-ligand coordination.[12]

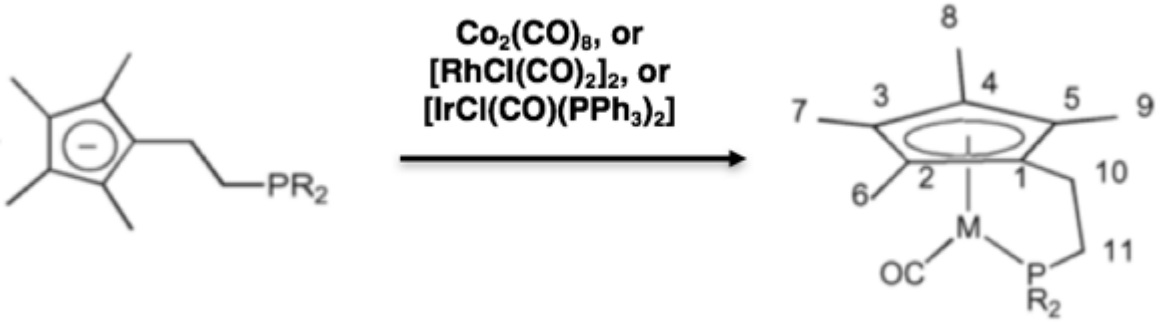

Scheme 1.4: Transmetallation of a Cp-phosphane ligand with $Co_2(CO)_8$, $[RhCl(CO)_2]_2$, or $[IrCl(CO)(PPh_3)_2]$.[11]

Moreover, a novel synthetic method was recently demonstrated for the preparation of MC ring complexes by employing ring-closing metathesis (RCM) reactions. Ogasawara *et al.* synthesized and reported a planar-chiral manganese-carbonyl ring complex with a Cp-phosphane ligand, *via* RCM to form the ring (2 in Scheme 1.5a).[4] This planar-chiral complex, (S)-2, which shows restricted rotation and constrained flexibility of the ligands, was found to be an effective chiral ligand for the rhodium-catalyzed asymmetric 1,2-addition reactions of phenylboronic acid to 1-naphthaldehyde (Scheme 1.5b) and phenylboroxine to arylaldehyde N-tosylimines (Scheme 1.5c) with high enantioselectivity.[4] Another derivative of MC ring complexes with π-arene ligand and chromium metal were also reported by the same group.[3]

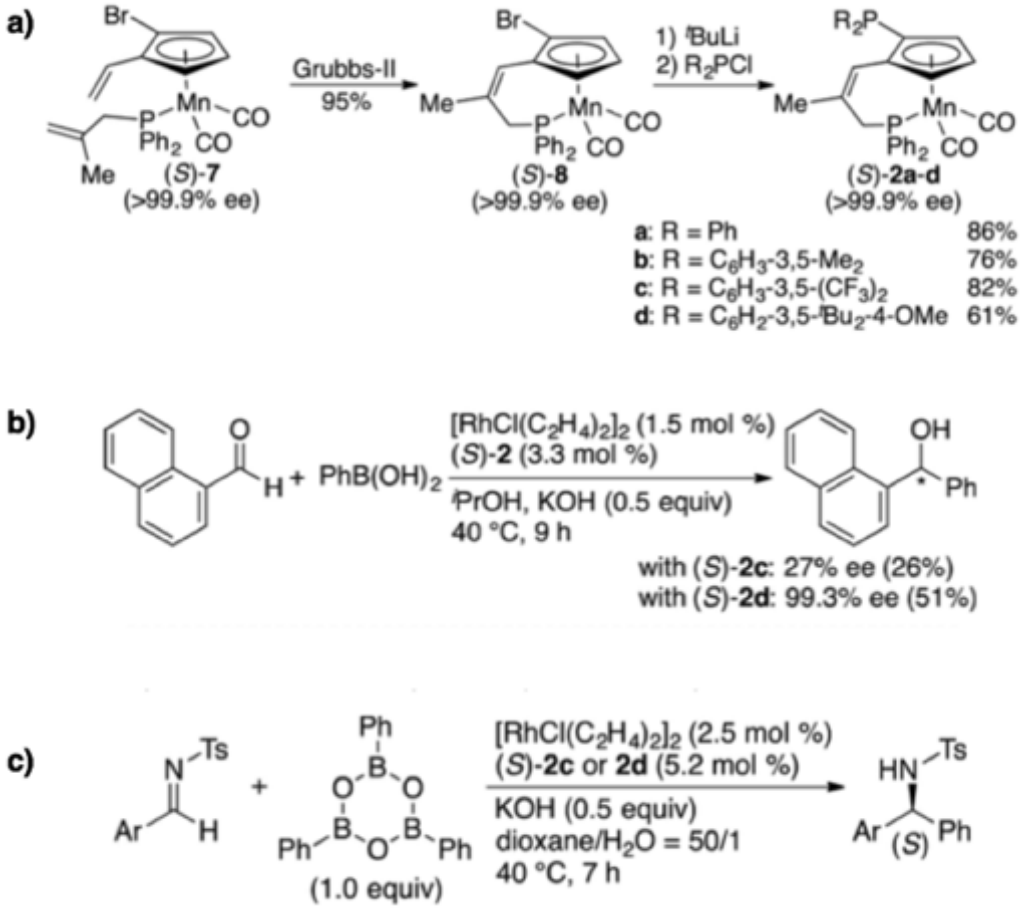

Scheme 1.5: Synthesis and applications of a manganese-carbonyl ring complex. a) Synthesis of planar-chiral manganese-carbonyl ring complex *via* RCM; Rhodium-catalyzed 1,2-addition reaction of b) phenylboronic acid, and c) phenylboroxine, by using (S)-2 as the chiral ligand.[4]

1.2 Introduction to Cyclic Polymers

The development of the synthesis and applications of polymers (or macromolecules) has been an ongoing research in the field for many years. Polymers with different architectures, such as linear, star, cyclic, graft, and hyperbranched, have been explored and developed, and their topological effects on polymer properties have also been widely studied. Cyclic polymers, which differ from linear polymers by the absence of end groups, can therefore exhibit very different properties and characteristics from their linear counterparts, and the effects of end group

functionality can also be investigated and studied. Some properties of cyclic polymers have been well-established, including higher glass transition temperature (T_g), smaller hydrodynamic volume, and smaller radius of gyration (R_g) as compared to their linear analogues.[17-19] Research interest in cyclic macromolecules has gained significant attention ever since the discovery of circular DNA in the 1960s, yet the development has remained fairly challenging mainly because of the difficulties in synthesizing pure and high MW cyclic polymers.[20-21] Recent progress has been achieved in controlled polymerization methods, organic coupling reactions, as well as characterization techniques, which have given rise to many research possibilities and opportunities in synthetic polymer chemistry and their potential applications as functional materials.

Crown ethers and cyclodextrins are cyclic oligomers that have been widely known for their applications in host-guest chemistry. They can be synthesized in different sizes, allowing them to coordinate with certain guests with high specificity at the interior of the ring to form stable complexes. Crown ethers are suitable for binding with specific alkali metal cations with high affinity for the oxygen atoms within the central cavity, such as 12-crown-4 for lithium cations, 15-crown-5 for sodium cations, and 18-crown-6 for potassium cations, as shown in Figure 1.4.[22]

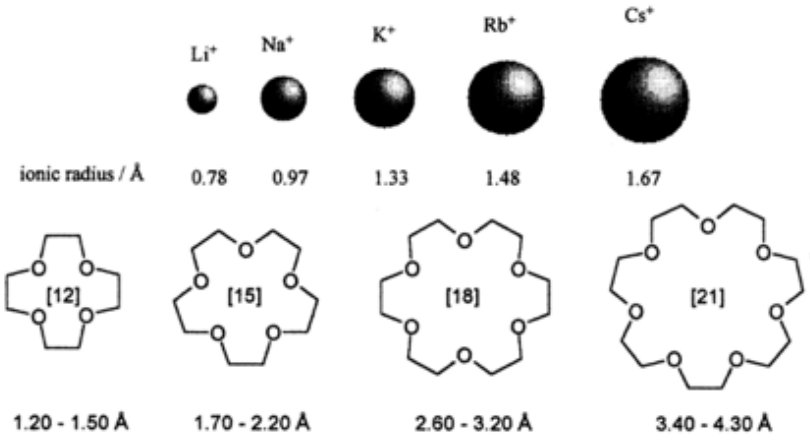

Figure 1.4: Ionic radius of alkali metal cations and the diameter of crown ether cavity.[22]

Cyclodextrins, on the other hand, are typically produced as α-cyclodextrin, β-cyclodextrin, and γ-cyclodextrin, which consists of 6, 7, and 8 repeating units of α-D-glucopyranose, respectively. The hydrophobic environment in the internal cavity of cyclodextrins allows specific host-guest interactions with lipophilic molecules, including amino acids, sugars, drugs, etc., primarily by van der Waals and hydrophobic interactions.[23] The host-guest interactions with cyclodextrin-based carriers have also led to successful applications in drug delivery.[24-25]

Moreover, macrocycles may be grafted using effective click reactions to generate grafted brush copolymers. For example, Zhang *et al.* reported the synthesis of a cyclic brush polymer by employing ring expansion metathesis polymerization (REMP), followed by a "grafting from" technique, as shown in Scheme 1.6.[26] Norborene-based functional monomers with a pendent hydroxyl group were used to construct the cyclic polymer backbone using REMP in the presence of a cyclic ruthenium-alkylidene catalyst UC-6, forming a cyclic polymer. The resulting cyclic polymer was then used as the macro-initiator for ROP of cyclic ester monomers to build the side-chain brushes. Some cyclic polymers have found important applications in biomedicine as drug carriers, with better bio-properties than their linear counterparts, such as a longer circulation time, higher tumor uptake, higher loading and faster release of anti-cancer drugs.[19]

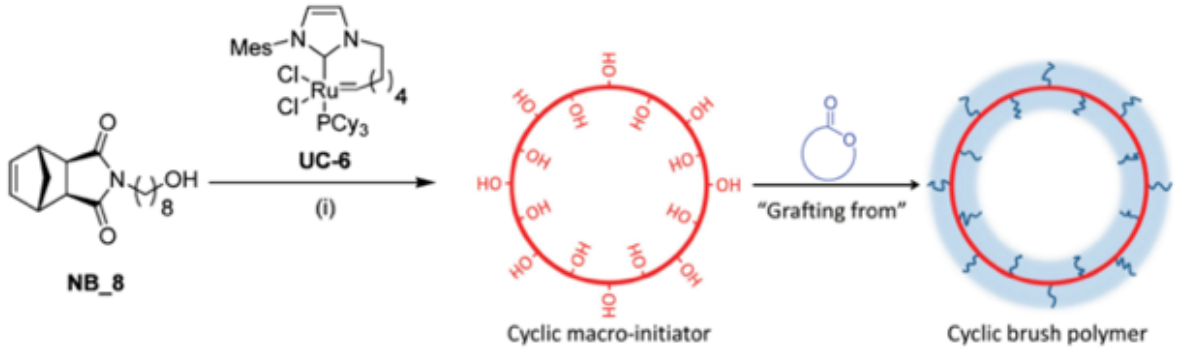

Scheme 1.6: Synthesis of cyclic brush polymer by REMP and a "grafting from" technique.[26]

1.2.1 Synthetic Routes for Cyclic Polymers

Traditionally, cyclic polymers can be synthesized by two major methods: ring-expansion and ring-closure methods. In ring-expansion polymerization, pure cyclic polymers with a broad range of MW are usually generated *via* the insertion of cyclic monomers into activated cyclic chains. However, the ring-expansion method often requires the use of cyclic initiators and/or cyclic monomers, which limits the types of systems that can be used for polymerization.[17,19]

For example, Grubbs *et al.* reported the synthesis of cyclic polybutadiene using ring opening metathesis polymerization (ROMP) of 1,5-cyclooctadiene, with a cyclic ruthenium (Ru) catalyst.[27] During the polymerization, the cyclic monomers are inserted into the activated cyclic Ru complex, where both ends of the growing chain are attached to the Ru metal center, forming a cyclic backbone (Scheme 1.7). The use of a cyclic Ru catalyst helps to construct and maintain the growing cyclic backbone during ROMP. In contrast, when an acyclic Ru catalyst was used, only linear polybutadiene was generated as there was only one chain end attaching to the Ru center.

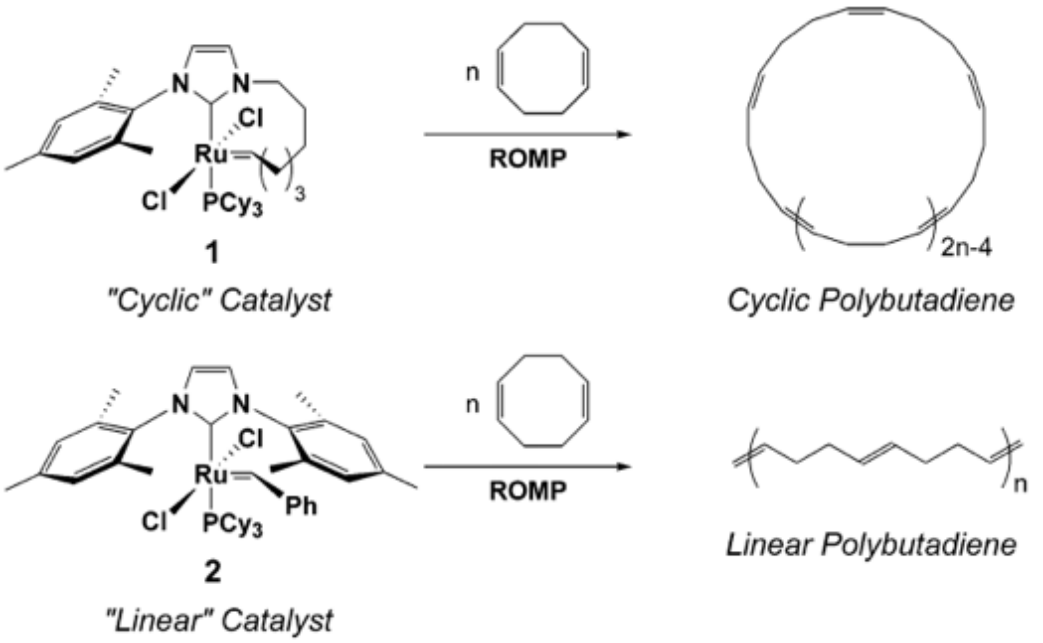

Scheme 1.7: ROMP of 1,5-cyclooctadiene using cyclic or acyclic catalyst.[27]

Ring-closure polymerization, on the other hand, involves an intermolecular polymerization to form linear chains with controlled MW, followed by an intramolecular coupling reaction of the functional end groups to close the ring. The ring-closure method has been widely used to synthesize cyclic polymers, as it is highly applicable and tolerant to a diversity of monomer systems and functional groups. However, diluted conditions are often required to facilitate the intramolecular ring-closure process, which can significantly affect the yield and purity of the cyclic polymeric products.[17-19] Itoh *et al.* reported the synthesis of cyclic polystyrene (PS) prepared by ring-closure technique, as shown in Scheme 1.8.[28] Similarly with other living polymerization, a linear PS chain with carboxyl and amino end groups were first prepared with a controlled MW. The resulting linear polymer, with a MW of *ca.* 1800 g/mol, was subsequently cyclized by an intramolecular coupling reaction between the functional end groups under highly diluted conditions. The cyclization was confirmed by the appearance of amide signals in the corresponding ^{13}C NMR and infrared (IR) spectra as a result of the end group coupling reaction.

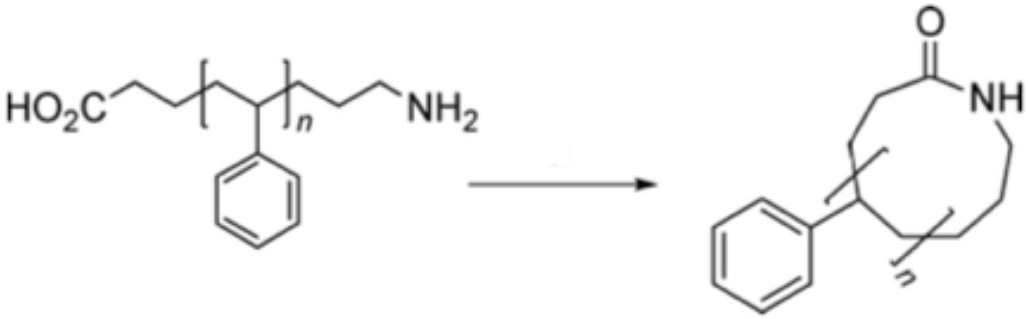

Scheme 1.8: Ring-closing polymerization of a linear PS chain.[28]

1.2.2 Metal-Containing Cyclic Oligomers

Ever since the successful synthesis of vinylferrocene in the 1950s, metal-containing polymers have become an interesting research topic in polymer chemistry.[29] Subsequently, vinylferrocene was polymerized *via* free radical polymerization to produce the first ferrocene-

containing polymer (Scheme 1.9). The introduction of the organometallic complexes into traditional organic polymers has offered new opportunities in the development of macromolecules with unique properties due to the presence of various metal complexes. Consequently, many studies focusing on the design of new synthetic metal-containing polymers by different polymerization techniques have been conducted. The development of metal-containing cyclic polymers has been explored by taking advantage of the unique geometries and properties of metal complexes, but still remained challenging because of the difficulties in synthesizing pure and high MW cyclic polymers.

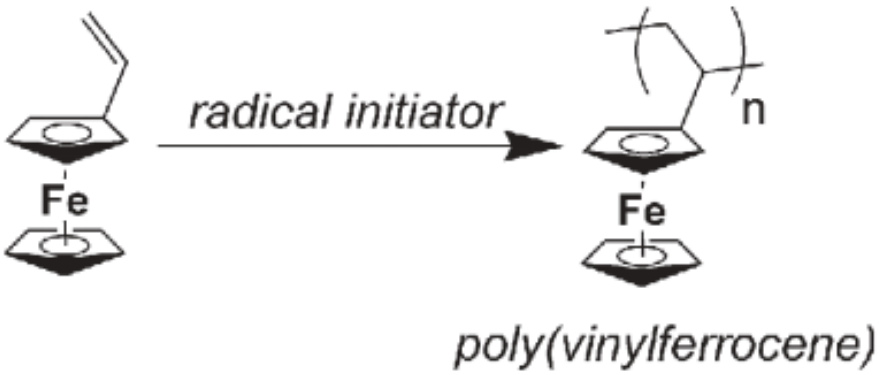

Scheme 1.9: Synthesis of polyvinylferrocene *via* radical polymerization.[29,30]

For example, Inkpen *et al.* reported the successful synthesis of oligomeric ferrocene ring ($[Fe(C_5H_4)_2]_n$, n = 5-7, 9) *via* Ullmann coupling reaction. The formation of ferrocene rings was attributed to the flexibility in the ring backbone, which was facilitated by the free rotation along the Cp-Fe bonds in ferrocene, as shown in Figure 1.5.[31] The cyclic oligomer for n = 6 was characterized by X-ray crystallography, which clearly showed the cyclic structure and geometry of the sample. This new class of ferrocene oligomer rings requires further studies for their potential applications in host-guest macromolecular interactions with neutral or charged guests.

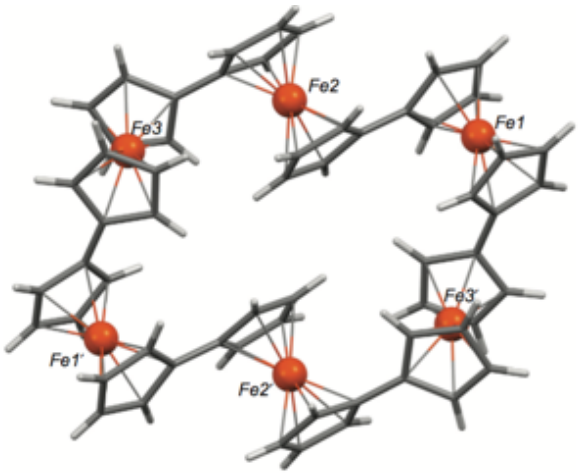

Figure 1.5: The X-ray crystal structure of a ferrocene ring (n = 6).[31]

1.2.3 Metal-Containing cyclic polymers

Moreover, Manners *et al.* reported the synthesis of cyclic poly(ferrocenyl-dimethylsilane) (PFS) in high yield and high MW by photocontrolled ROP in the presence of a neutral Lewis donor, 4,4'-dimethyl-2,2'-bipyridine (Me_2bpy), as the initiator.[32] In fact, when other initiators such as 1,2-bis(diphenylphosphino)ethane and $Na[C_5H_5]$ were used, no cyclic polymers were produced. They suggested that the cyclic structure was promoted by the weak interactions of Me_2bpy at the soft iron center, which allowed the reactive Cp anion end group in the growing PFS chain to backbite the other chain-end to complete the ring-closing process (Scheme 1.10). During ROP, several possible products were generated, including cyclic polymers, cyclic oligomers, and linear polymers. The ratio of the products could be adjusted by varying the polymerization conditions, in which the production of high MW cyclic PFS was favored when a higher initial concentration, longer irradiation time, and lower temperature were used. The cyclic polymeric products were isolated by fractional precipitation, and they were subsequently measured by gel permeation chromatography (GPC). The highest M_n obtained was 182,900 g/mol, with a degree of polymerization (DP) of 756 repeating units and a polydispersity index (PDI) of 1.2. The successful

synthesis of metal-containing macrocycles with a high MW indicated that the binding strength of the initiator, the structural and geometric effect of the monomers, as well as the unrestricted rotation of the Cp-Fe bonds, play significant roles in the synthesis of large cyclic polymers.[32]

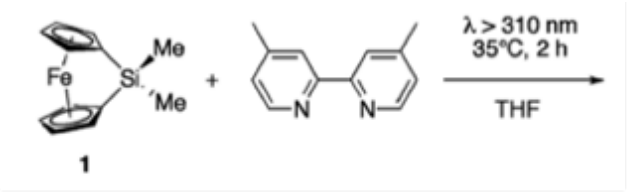

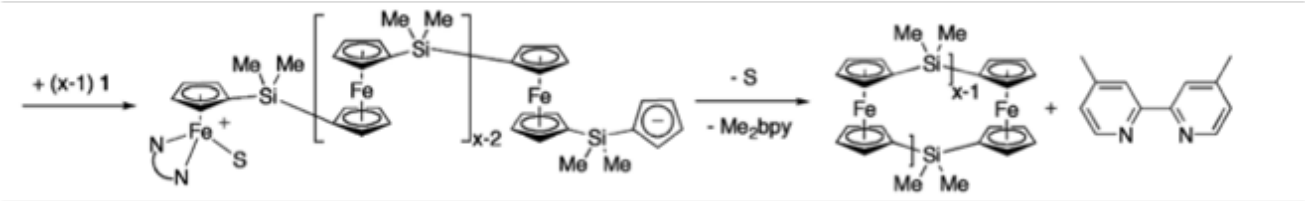

Scheme 1.10: Synthesis of cyclic PFS *via* intramolecular backbiting reaction.[32]

1.2.4 Characterization Methods

Polymers are typically characterized by their size and topology as fundamental analysis. While the polymer size, including MW and PDI, can be easily measured by GPC, the polymer topology can be difficult to verify. For cyclic polymers, their cyclic topology has been determined and confirmed by numerous techniques, such as GPC, end group analysis, and microscopic analysis. Specific examples will be given and discussed below.

1.2.4.1 Gel Permeation Chromatography

GPC is a common technique for measuring the PDI and MW of polymers. It separates the analytes based on their size (or hydrodynamic volume, V_h), whereby smaller samples are retained by passing through the pores in the column, resulting in a longer retention time and a larger elution volume. It is commonly known that cyclic polymers display smaller V_h than their linear counterparts of the same MW, because of the confined conformation of cyclic polymers. As a result, cyclic polymers should exhibit a longer elution time in GPC than their linear analogues of

the same MW. For example, Xie *et al*. compared the retention time of linear $PBNP_{20}$-(b-$PTNP_{20}$)$_2$ with cyclic $PBNP_{10}$-(b-$PTNP_{20}$)$_2$-b-$PBNP_{10}$ by GPC.[33] The results in Figure 1.6 clearly show the retention time difference between the linear and cyclic polymers, in which the cyclic polymers were eluted later than the linear polymer because of this smaller V_h. Indeed, many other cyclic polymer systems have also yielded similar and consistent results.[32] GPC has therefore been widely used as one of the confirmation techniques to suggest cyclic topology, by comparing the retention time or elution volume for the linear and cyclic polymers.

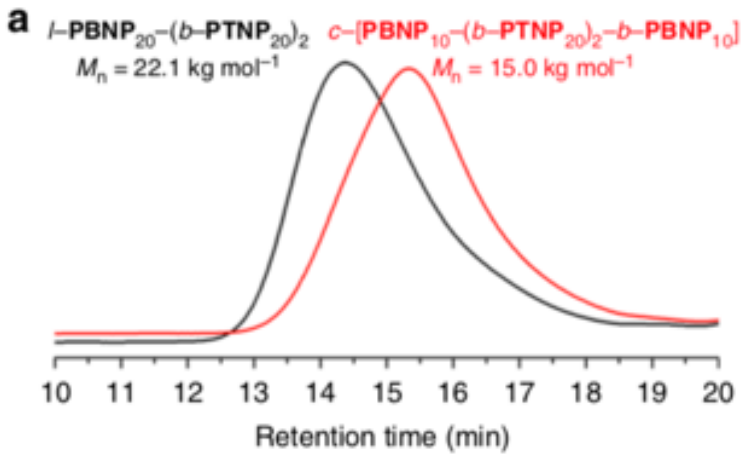

Figure 1.6: GPC traces of linear $PBNP_{20}$-(b-$PTNP_{20}$)$_2$ and cyclic $PBNP_{10}$-(b-$PTNP_{20}$)$_2$-b-$PBNP_{10}$.[33]

1.2.4.2 End Group Analysis

Due to the advanced development of instrumentations in characterization, functional end groups can be easily analyzed and identified by numerous techniques, such as NMR spectroscopy, IR spectroscopy, and mass spectroscopy (MS). Polymers with distinct end group signals can even be integrated with the repeating units for the determination of the average DP of the polymer in ^{1}H NMR. However, this end group analysis by ^{1}H NMR method can only be applied to polymer systems with low MW typically below 20,000 g/mol. This is because as the MW increases, the

signal for the repeating units will become broad and large, whereas the end group signals might not be visible for integration because of poor resolution. Besides, new functional groups can often be formed during ring-closing reactions between two reactive end groups, and the corresponding signals can also be observed in NMR and IR spectra. As previously discussed, Itoh *et al*. reported the synthesis of cyclic PS by a ring-closure technique (Scheme 1.8).[28] The cyclization was confirmed by the appearance of amide group signals in ^{1}H NMR, ^{13}C NMR and IR spectra, as a result of the intramolecular end group coupling reaction between the carboxyl and amino groups.[28] Moreover, matrix-assisted laser desorption ionization-time of flight (MALDI-TOF) MS could also be used to distinguish linear and cyclic polymers based on their masses. Cyclic polymers, due to the absence of end groups, will show a mass difference corresponding to the end groups from their linear analogues. Figure 1.7 shows the overlay of MALDI-TOF spectra for linear PFS (in black) and cyclic PFS (in red) produced by Manners *et al.* The distance between each peak of the same color corresponds to the mass of each repeating unit. The overlay spectrum also showed distinct shifts (in red) for the cyclic polymer, due to the absence of end groups. [32]

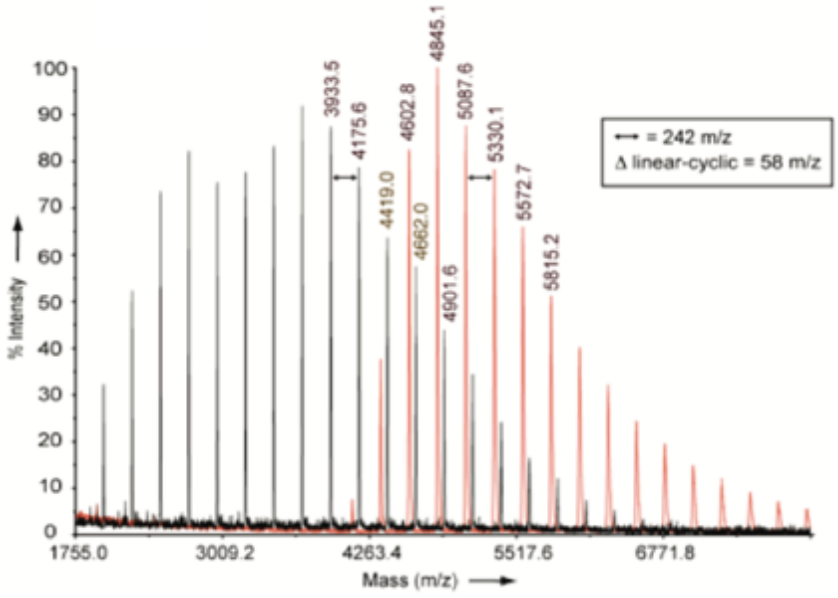

Figure 1.7: Overlay MALDI-TOF spectra for linear (in black) and cyclic (in red) PFS.[32]

1.2.4.3 Atomic Force Microscopy

Atomic force microscopy (AFM) is a microscopic technique that can provide information about the surface topography and surface properties of samples. It uses a cantilever with a sharp tip to scan over a sample surface, where the interaction between the tip and the sample surface causes cantilever deflections. These deflections are detected with a laser beam and converted into topographic profiles and images for analysis.[34] Due to the toroidal shape of cyclic polymers, which can lead to an uneven surface between the cyclic backbone and the hole, AFM has been utilized to provide strong evidence for cyclic polymer topology.[33,35-38] For example, Schappacher and Deffieux reported a macrocyclic copolymer brush, PCEVE-PS, by an intramolecular cyclization of PCEVE linear chain, followed by post-functionalization with PS brushes.[35] The cyclic structure was confirmed by AFM as shown in Figure 1.8b, which shows clear toroidal shapes for the sample. Uncyclized PS-brushes, which appeared as worm shapes, were also observed in the crude sample as shown in the AFM image (Figure 1.8a), which provided a clear differentiation between the images for the linear and cyclic products (Figure 1.8b).

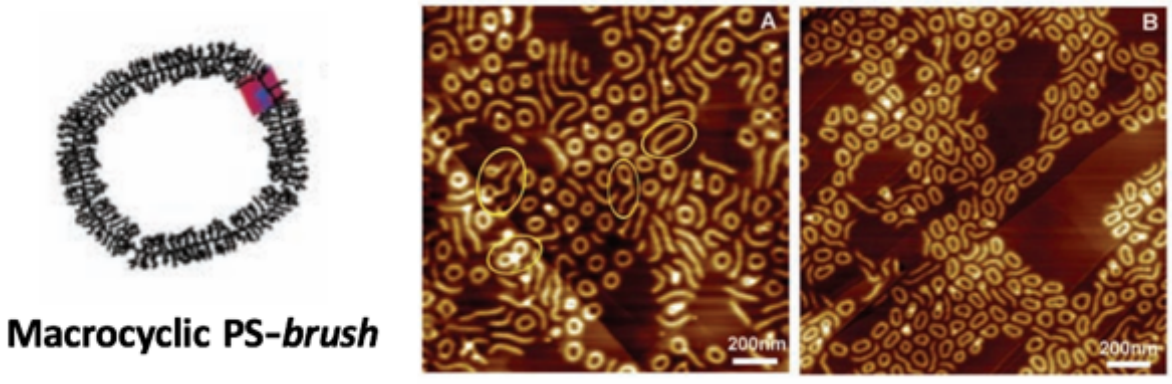

Figure 1.8: AFM images for a) crude, and b) fractionated PCEVE-PS cyclic polymer brushes.[35]

Moreover, Xie *et al*. reported a POSS-modified cyclic polymer, c-[$PBNP_{10}$-(b-$PTNP_{160}$)$_2$-b-$PBNP_{10}$]-POSS, and demonstrated the polymer cyclic topology using AFM.[33] The AFM images

(Figure 1.9a and 1.9b) show some evenly distributed toroidal-shaped samples with inner and outer diameters of 25-35 nm and 8-12 nm, respectively. The 3D plot for the sample (Figure 1.9c) shows height signals ranging from 0.6-0.8 nm, and the corresponding profile analysis (Figure 1.9d) shows 2 peaks, caused by uneven forces on the sample surface due to the presence of toroidal-shaped polymer backbones. These AFM results provided a strong evidence for the formation of the cyclic topology.

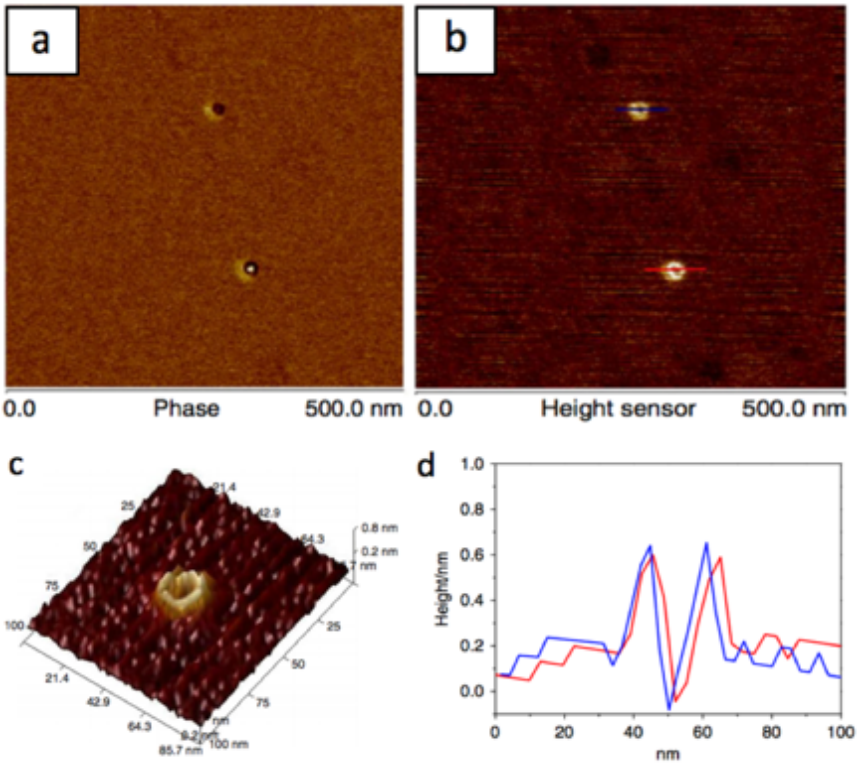

Figure 1.9: AFM a) phase and b) height images, c) 3D plot of toroidal shape, and d) profile analysis for c-[$PBNP_{10}$-(b-$PTNP_{160}$)$_2$-b-$PBNP_{10}$]-POSS.[33]

1.2.4.4 Transmission Electron Microscopy

Transmission electron microscopy (TEM) is a microscopic technique that transmits electron beams through a thin specimen to form high resolution images. It has been widely used in chemical and biological research to visualize the structure of macromolecules and nanoparticles.

As previously described, Xie *et al.* reported a POSS-modified cyclic polymer, c-[$PBNP_{10}$-(b-$PTNP_{160}$)$_2$-b-$PBNP_{10}$]-POSS, where the cyclic topology was also confirmed by TEM.[33] The corresponding TEM images in Figure 1.10 clearly show the cyclic topology of the POSS-modified cyclic polymer, with inner and outer diameters of about 25-35 nm and 10-14 nm, respectively. The outer ring appears to be brighter, representing the cyclic polymers due to low electron density, whereas the inner ring appears darker, representing the POSS moieties because of the higher electron density distribution in POSS (Figure 1.10). The ring sizes also matched with the theoretical calculated DP, which clearly confirmed the cyclic topology.

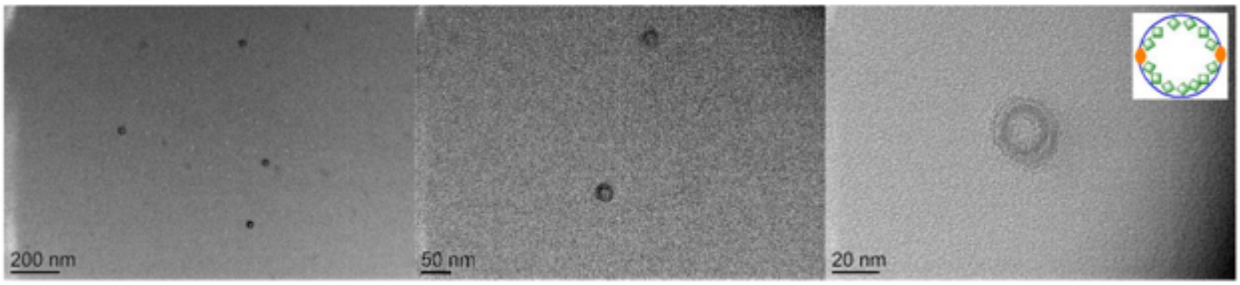

Figure 1.10: TEM images c-[$PBNP_{10}$-(b-$PTNP_{160}$)$_2$-b-$PBNP_{10}$]-POSS in $CHCl_3$ at 0.001 mg/mL.[33]

1.3 Migratory Insertion Reaction

Migratory insertion reactions (MIRs), which indicate the formation of a new anionic ligand by the combination of an adjacent anionic ligand and a neutral ligand, often occur in organometallic complexes. This rearrangement decreases the overall electron count of the organometallic complex by two, providing an empty orbital on the metal (Scheme 1.11). This allows the formation of a new bond between the metal and another nucleophilic ligand. In an alkyl dicarbonyl cyclopentadienyl iron complex ($CpFe(CO)_2R$ or FpR), MIR occurs via CO insertion. The anionic alkyl group on the FpR complex migrates to the CO group, forming an intramolecular

acyl bond and an empty orbital on the iron center (Scheme 1.11). For example, MIR between FpR and a nucleophilic phosphane ligand generated an air-stable Fe-P bonded complex.[39]

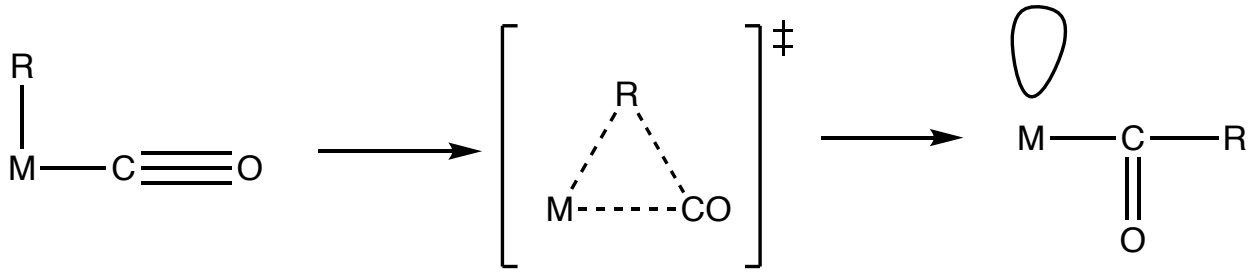

Scheme 1.11: General scheme for MIR *via* CO insertion.

1.3.1 Migration Insertion Polymerization of FpP

Our group previously developed migration insertion polymerization (MIP) by adopting the MIR mechanism, and reported the synthesis of a heterobifunctional AB-type monomer for MIP using a Fp complex and a nucleophilic phosphane ligand as the functional groups.[40] The monomer, cyclopentadienyl dicarbonyldiphenylphosphinopropyl iron (FpP), was synthesized by a salt elimination reaction between cyclopentadienyl dicarbonyl iron potassium (FpK) and 1-chloropropyldiphenylphosphide (Scheme 1.12). Subsequently, FpP can undergo MIP at an elevated temperature, without the use of any initiators or solvents, to form the polymer, poly(cyclopentadienyl carbonyl diphenylphosphinobutanoyl iron) (PFpP). PFpP is soluble in various organic solvents and displays narrow MW distributions, with a highest M_n of about 12,000 g/mol and a PDI of 1.28.[40] The development of MIP can offer new possibilities for synthesizing novel metal-containing polymers, by incorporating various metal complexes and ligands for new functional materials. MIP can also be performed at high monomer concentration or even in bulk, which could be a practical method in the industry.

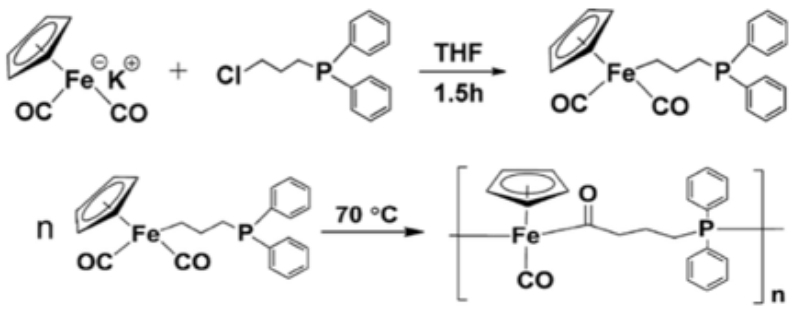

Scheme 1.12: Synthesis and MIP of FpP.[40]

Wang *et al*. continued to study the polymerization conditions for MIP, and they found that the reaction for FpP polymerization was concentration- and temperature-dependent (Figure 1.11).[41] At low monomer concentration (1% by weight), FpP underwent intramolecular MIR to form cyclized products. In contrast, intermolecular MIR was favored to form PFpP when the FpP concentration was increased to 10% by weight. Moreover, MIR was only observed when the reaction was performed at high temperature (70 °C).[41] In summary, this study showed that MIP of FpP requires both a high monomer concentration (10 wt. %) and a high reaction temperature (70 °C) to generate PFpP.

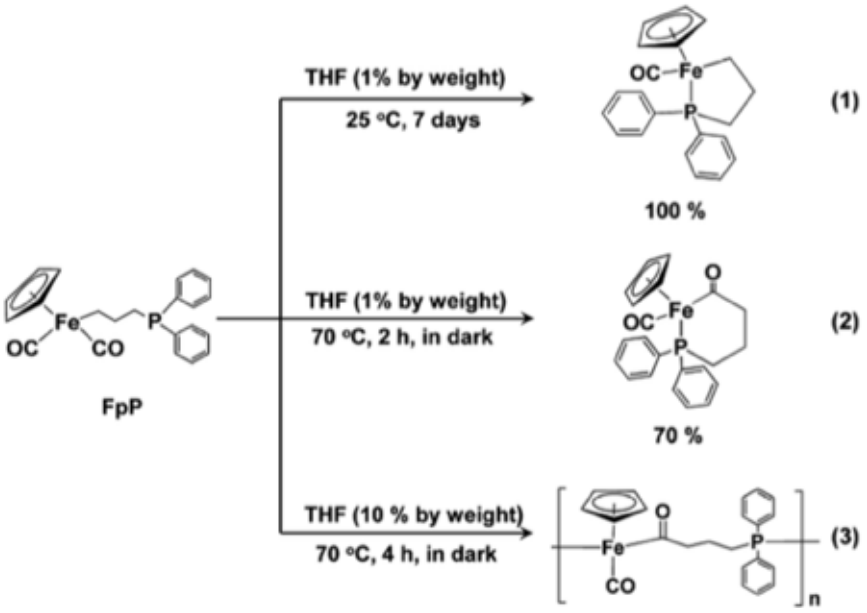

Figure 1.11: Reactions of FpP in THF.[41]

^{1}H, ^{31}P NMR, and IR spectroscopies were used for PFpP characterization. After MIP, the ^{31}P NMR spectrum of PFpP revealed three peaks at 73 ppm, 72 ppm, and -14 ppm (Figure 1.12). The major peak at 73 ppm represents the Fe-P bonds in the polymer chain, while the peaks at 72 ppm and -14 ppm represent the iron-coordinated and uncoordinated phosphane end group respectively. The IR spectrum showed two CO absorption signals at 1910 cm^{-1} and 1600 cm^{-1}, which can be assigned to the terminal CO and acyl CO groups, respectively, confirming that CO insertion had occurred during MIP.[40]

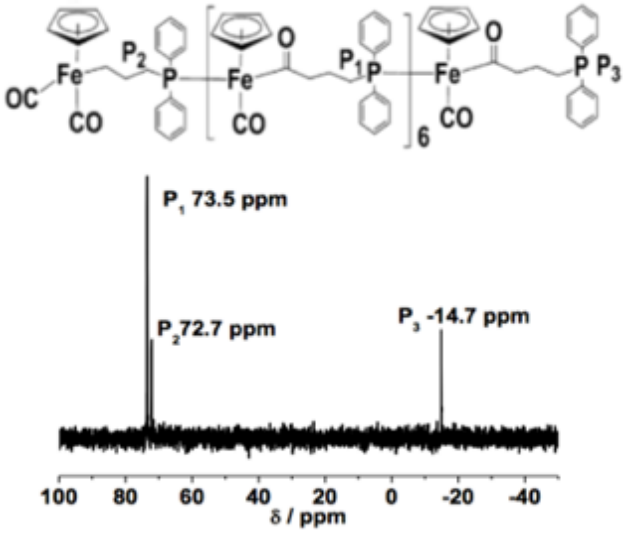

Figure 1.12: The ^{31}P NMR spectrum for PFpP. [40]

1.3.2 Migration Insertion Polymerization of ^{P}FpR

The solvent system also plays an important role in the polymer structure obtained. Wang *et al*. reported that the MIP of FpP in tetrahydrofuran (THF) produced linear PFpP, whereas a cyclic PFpP was generated in THF/hexane mixed solvents. THF, a good solvent for PFpP, extended the PFpP chain, favoring a linear structure. However, in a THF/hexane mixture, in which hexane is a poor solvent, a cyclic conformation of PFpP was obtained due to chain contraction.[42] It was rationalized that the rigid metal bonds of PFpP prevented the cyclic conformation in the good solvent. As a result, a modification on the monomer was made in our group, and the Cp

ligand was incorporated into the backbone, which consists of Fe-Cp-P (P = propyldiphenylphosphane) bonds with a bond angle of approximately 90°. The modified monomers, alkyl dicarbonyl diphenylphosphinopropylcyclopentadienyl iron (^{P}FpR), for R = CH_3 and $(CH_2)_5CH_3$, were designed and synthesized for ring-closing MIP (Scheme 1.13a).[43] The resulting polymers, P(^{P}FpR), were confirmed to adopt a cyclic structure by TEM (Figure 1.13a), AFM (Figure 1.13b), and ^{31}P NMR spectroscopy (Figure 1.13c) with the absence of end group signals. Cyclic formation was attributed to the non-linear, piano-stool geometry of ^{P}FpR, as well as the low rotation barrier of the Cp ring, which provided the backbone chain with flexibility to generate cyclic P(^{P}FpR) (Scheme 1.13b).[43]

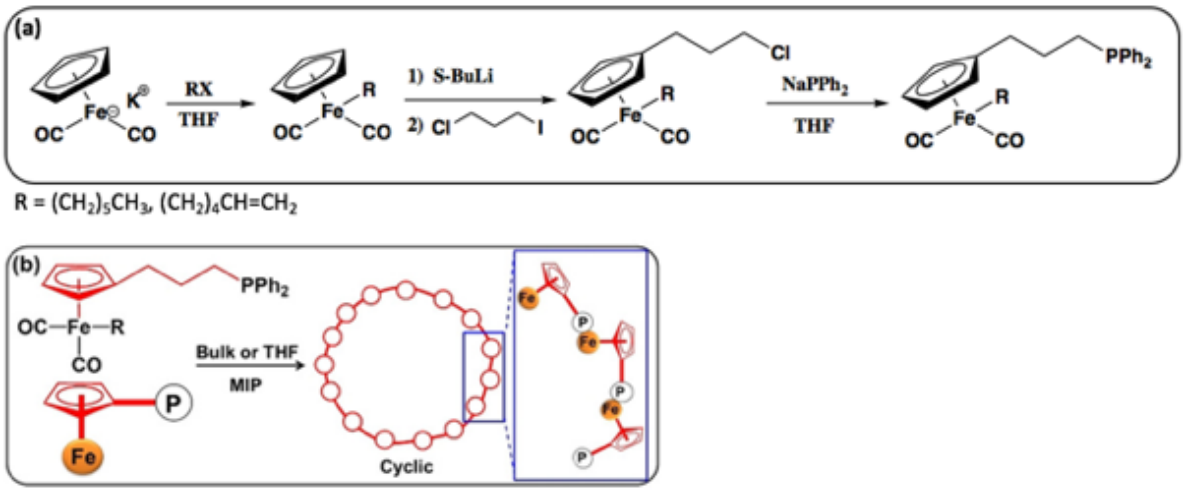

Scheme 1.13: Synthetic scheme (a) and MIP (b) of ^{P}FpR.[43]

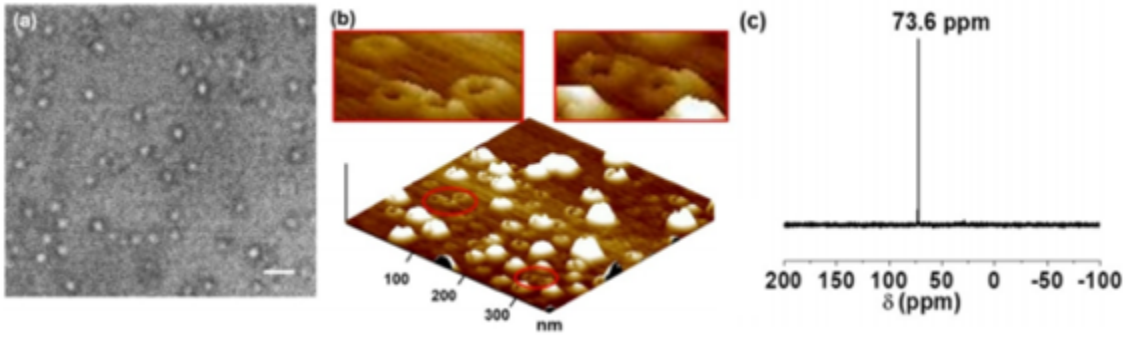

Figure 1.13: a) TEM and b) AFM images of macrocycles; c) ^{31}P NMR spectrum for ^{P}FpR.[43]

2.0 Experimental

2.1 Materials and Instrumentation

Materials: 1-bromohexane (98%), 1-chloro-3-iodopropane (99%), 6-chloro-1-hexene (96%), benzophenone (99%), *sec*-butyllithium solution (1.4 M in cyclohexane), cyclopentadienyl iron(II) dicarbonyl dimer (Fp_2, 99%), potassium (chunks, 98%), and sodium were purchased from Sigma Aldrich. Chlorodiphenylphosphine (>97.0%) was purchased from Tokyo Chemical Industry. All chemicals were used as received unless otherwise indicated. THF was freshly distilled over sodium/benzophenone under nitrogen before use.

Instrumentation: ^{1}H, ^{13}C and ^{31}P NMR, ^{1}H-^{1}H correlation spectroscopy (COSY), and ^{13}C-^{1}H heteronuclear multiple quantum coherence (HMQC) 2D NMR were recorded on a Bruker Avance 300 (300 MHz) spectrometer at ambient temperature using $CDCl_3$ as the solvent. ^{1}H NMR chemical shifts were reported relative by the residual $CDCl_3$ signal, and ^{31}P NMR resonances were referenced to an external standard sample of 85% H_3PO_4. TEM images were obtained on a transmission electron microscope (Philips CM10) with an acceleration voltage of 60 kV. TEM samples were prepared by adding 10 μL of sample in THF solution (5 mg/mL) on a carbon-coated copper grid. The copper grid was dried overnight at room temperature. MS were acquired by performing positive ion electrospray ionization (ESI) on a Thermo Scientific Q-Exactive Orbitrap mass spectrometer. Samples were infused at 10 μL/min in acetonitrile (ACN). Fourier-transform infrared (FT-IR) spectra were recorded on a Thermo Scientific Nicolet 5700 spectrometer with a resolution of 0.4 cm^{-1}. Elemental analyses were carried out using a Vario EL cube on an elemental analyzer (Elementar). GPC analyses were carried out using two instruments: 1) A Viscotek VE 2001 GPC instrument equipped with PolyAnalytik SupeRes mixed bed columns and a TDA 305 triple detector array (differential refractive index, light scattering, and viscosity), using THF as

eluent. The temperature was set at 35 °C and held constant with a flow rate of 1 mL/min; 2) An Agilent 1100 Series GPC module equipped with two Jordi Resolve DVB medium mixed bed columns and a Waters 410 differential refractometer using dimethylformamide (DMF, with 0.1% lithium chloride) as the eluent. The columns were maintained at 45 °C and held constant with a flow rate of 0.9 mL/min. Single crystals suitable for X-ray diffraction analysis were mounted onto the tip of glass fibers with paratone oil and transferred immediately into the cold nitrogen gas stream of the diffractometer cryostat. X-ray data were collected using Mo-Kα radiation (λ = 0.71073 Å) at 200 K on a Bruker Kappa APEX II diffractometer (Madison, WI, USA).

2.2 Synthesis of P(FpP)

Linear polymer P(FpP) was prepared *via* MIP of the FpP monomer, as described in a previous report (Scheme 2.1).[40] The preparation of FpK, PPh_2Na, $Ph_2P(CH_2)_3Cl$, and FpP will be described in this section.

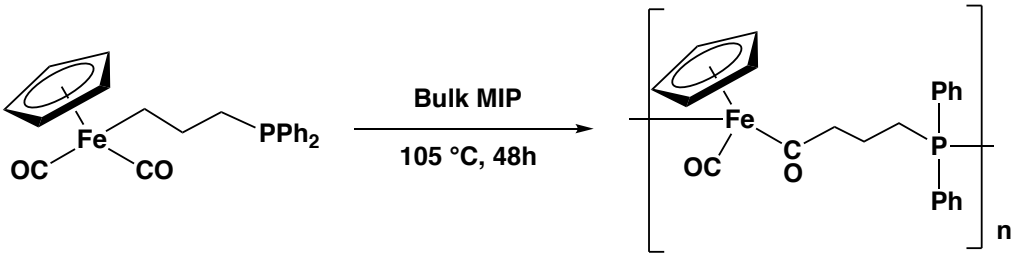

Scheme 2.1: Synthesis of P(FpP).

2.2.1 Synthesis of FpK

Potassium benzophenone ketyl was prepared by stirring 1.0 molar equivalent (eq) of benzophenone (5.00 g, 27.5 mmol) and 1.0 eq of potassium metal (1.07 g, 27.5 mmol) in a Schlenk round bottom (RB) flask containing distilled THF (50 mL), as shown in Scheme 2.2. The solution was stirred overnight to ensure complete reaction. Afterwards, 0.55 eq of Fp_2 dimer (5.35 g, 15.1 mmol) was added to the solution and stirred for 2 hours at room temperature to produce FpK. THF

was subsequently removed after the reaction, and the crude product precipitate was washed with degassed toluene 3 times. The supernatant was removed *via* cannula. The product was dried under vacuum yielding an orange powder. Yield: 5.27 g (89 %).

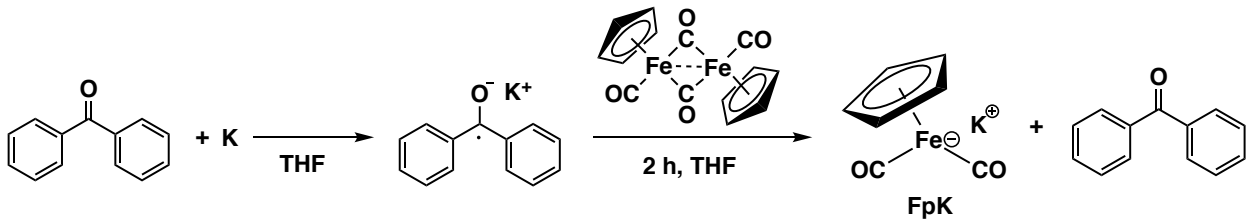

Scheme 2.2: Synthesis of FpK.

2.2.2 Synthesis of Sodium Diphenylphosphide (PPh_2Na, 0.5 M in THF)

PPh_2Na was prepared by heating 1.0 eq of chlorodiphenylphosphine ($ClPPh_2$, 18.5 mL, 0.1 mol) with 3.0 eq of sodium metal (6.9 g, 0.3 mol) in a Schlenk RB flask containing distilled THF (200 mL) (Scheme 2.3). The mixture was stirred at 40 °C for 3 days, resulting in a bright red/orange solution. The solution was used directly without purification for further reactions. ^{31}P NMR (THF): -24 ppm.

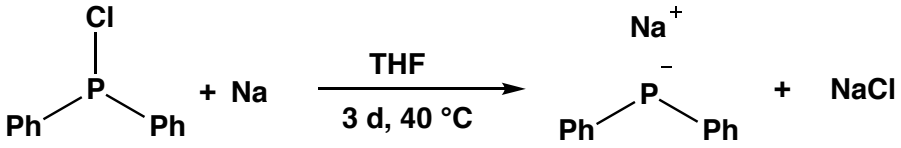

Scheme 2.3: Synthesis of PPh_2Na.

2.2.3 Synthesis of (3-chloropropyl)diphenylphosphane ($Ph_2P(CH_2)_3Cl$)

As shown in Scheme 2.4, 1.0 eq of PPh_2Na (0.5 M, 25 mL, 12.5 mmol) was added dropwise to a distilled THF solution (25 mL) containing 1.75 eq of 1-bromo-3-chloropropane (2.16 mL, 21.9 mmol) at 0 °C with stirring. The reaction mixture was stirred overnight. After the reaction the THF was removed, and the crude product was subsequently purified by running a silica-gel column

with degassed hexane. The eluent was collected in fractions, and the products were monitored by thin layer chromatography. The final product was concentrated under vacuum, yielding a colorless oil. ^{1}H NMR ($CDCl_3$): 7.50-7.21 ppm (m, 10H, $C_6\mathbf{H}_5$), 3.61 ppm (t, 2H, $C\mathbf{H}_2Cl$), 2.18 ppm (m, 2H, $C\mathbf{H}_2PPh_2$), 1.88 ppm (m, 2H, $CH_2(C\mathbf{H}_2)CH_2$), 31P NMR ($CDCl_3$): -16.1 ppm (uncoordinated phosphine). Yield: 3.05 g (93%).

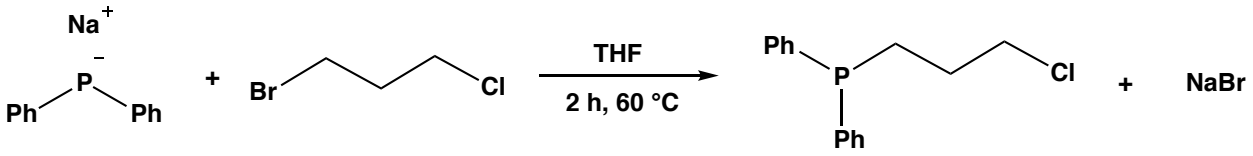

Scheme 2.4: Synthesis of $Ph_2P(CH_2)_3Cl$.

2.2.4 Synthesis of FpP

In a Schlenk RB flask containing FpK (2.26 g, 10.4 mmol) and distilled THF (50 mL), 1.2 eq of $Ph_2P(CH_2)_3Cl$ (3.3 g, 12.6 mmol) was added dropwise to the FpK solution at 0 °C (Scheme 2.5). The reaction was stirred in the dark for 1.5 hours at room temperature. The THF was subsequently removed, and the crude product was purified and filtered through a silica-gel column using hexane/dichloromethane (DCM) (4 : 1, v/v) as eluent. The first yellow band was collected and the solvent was removed under vacuum, yielding a yellow oil. ^{1}H NMR ($CDCl_3$): 7.41-7.24 ppm (m, 10H, $C_6\mathbf{H}_5$), 4.65 ppm (m, 5H, $C_5\mathbf{H}_5$), 2.09 ppm (t, 2H, $C\mathbf{H}_2PPh_2$), 1.54 (s, 4H $Fe(C\mathbf{H}_2)_2CH_2PPh_2$), ^{31}P NMR ($CDCl_3$): -15.6 ppm (uncoordinated phosphine). Yield: 1.27 (30%).

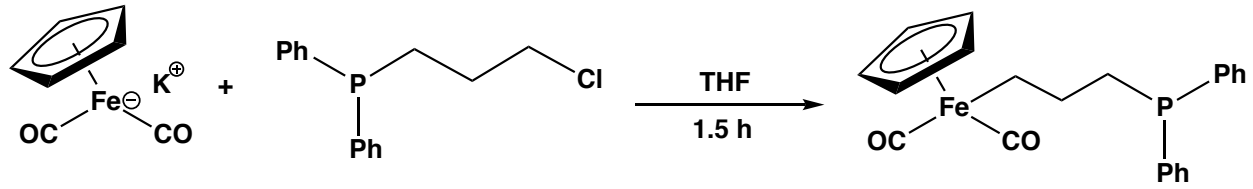

Scheme 2.5: Synthesis of FpP.

2.2.5 Synthesis of P(FpP)

In a Schlenk reaction flask containing FpP (1.25 g, 3.1 mmol), bulk MIP was initiated by heating the reaction flask to 105 °C. After 48 hours, the polymerization was terminated by cooling to room temperature. The MIP crude product was dissolved in a small amount of THF (5 mL) and precipitated into hexane (200 mL). The polymer was separated *via* filtration and washed with hexane 3 times to remove impurity traces. The precipitates were dried under vacuum for 24 hours, yielding yellow powders. Yield: 900 mg (72%). ^{1}H NMR ($CDCl_3$): 7.78-7.24 ppm (b, 10H, C_6H_5), 4.43-4.27 ppm (b, 5H, C_5H_5), 2.78-2.60 ppm (b, 1H, $COCH_2$), 2.47-2.17 ppm (b, 1H, $COCH_2$), 2.13-1.89 ppm (b, 2H, CH_2PPh_2), 1.32-0.74 (b, 2H, $CH_2(CH_2)CH_2$). ^{31}P NMR ($CDCl_3$): 72 ppm (coordinated Fe-P bonds in main group), 71 ppm (coordinated Fe-P bond in the end group), 33 ppm (uncoordinated oxidized P=O bond).

2.3 Synthesis of ^{P}FpR

^{P}FpR, $[\eta^5\text{-}(C_6H_5)_2P(CH_2)_3C_5H_4]Fe(CO)_2R$, was prepared *via* a 3-step reaction according to our previous report (Scheme 2.6).[43] ^{P}FpR, for which R = $(CH_2)_5CH_3$ (**a**) or $(CH_2)_4CH{=}CH_2$) (**b**) were prepared as monomers for MIP. The detailed experimental procedures for each step will be described hereafter.

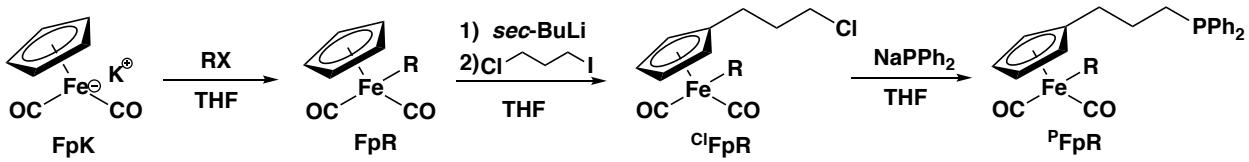

Scheme 2.6: Synthetic scheme for the preparation of ^{P}FpR. RX = alkyl halide; **a** = $Br(CH_2)_5CH_3$ and **b** = $Cl(CH_2)_4CH{=}CH_2$.

2.3.1 Synthesis of FpR, $[\eta^5\text{-}C_5H_5]Fe(CO)_2R$, R = $(CH_2)_5CH_3$ or $(CH_2)_4CH{=}CH_2$)

In a distilled THF solution (50 mL) containing 1.0 eq of FpK (3.85 g, 17.9 mmol), 0.9 eq of alkyl halide, $CH_3(CH_2)_5Br$ for **a** (2.65 g, 16.1 mmol) or $CH_2{=}CH(CH_2)_4Cl$ for **b** (1.91 g, 16.1 mmol), was added to the solution dropwise at 0 °C. After the addition, the reaction mixture was warmed to room temperature and stirred for another 2 hours. THF was then removed, and the crude product was dissolved in a small amount of hexane and passed through a Celite column to remove salts. The crude product was further purified by running a silica-gel column, using hexane as eluent. The yellow band, which contained the FpR product, was collected and hexane was removed under vacuum to yield a yellow oil. For **a**, $Fp(CH_2)_5CH_3$: ^{1}H NMR ($CDCl_3$): 4.71 ppm (s, 5H, $C_5\mathbf{H}_5$), 1.43-1.26 ppm (10H, $Fe(C\mathbf{H}_2)_5CH_3$), 0.86 ppm (3H, $(CH_2)_5C\mathbf{H}_3$). Yield: 3.52 g (83%). For **b**, $Fp(CH_2)_4CH{=}CH_2$: ^{1}H NMR ($CDCl_3$): 5.79 ppm (ddt, J = 17.1 Hz, 10.1 Hz, 6.8 Hz, 1H, $Fe(CH_2)_4C\mathbf{H}{=}CH_2$), 5.00-4.89 ppm (m, 2H, $Fe(CH_2)_4CH{=}C\mathbf{H}_2$), 4.71 ppm (s, 5H, $C_5\mathbf{H}_5$), 1.53-1.43 ppm (8H, $Fe(C\mathbf{H}_2)_4CH{=}CH_2$). Yield: 3.68 g (88%).

2.3.2 Synthesis of ^{Cl}FpR, $[\eta^5\text{-}Cl(CH_2)_3C_5H_4]Fe(CO)_2R$

In a distilled THF solution (100 mL) containing 1.0 eq of FpR (**a**: 3.55 g, 13.5 mmol; **b**: 3.68 g, 14.1 mmol), 1.5 eq of *sec*-butyllithium (1.4 M in cyclohexane; **a**: 14.5 mL, 20.3 mmol; **b**: 15.2 mL, 21.2 mmol) was added dropwise at -78 °C and stirred for 10 minutes. 1.7 eq of 1-chloro-3-iodopropane (**a**: 2.5 mL, 23 mmol; **b**: 2.6 mL, 24.1 mmol) was added dropwise to the solution mixture at -78 °C while stirring. The solution was warmed to room temperature and stirred for 1.5 hours. THF was removed after the reaction, the crude product was re-dissolved in a small amount of hexane, and passed through a Celite column to remove LiI salts. The crude product was further purified by silica-gel column chromatography using hexane as the eluent. After the separation of a yellow band was observed, a mixture of hexane/DCM (3:1 v/v) was then used as eluent to

separate the yellow bands. The second yellow band was collected and concentrated under vacuum, yielding a yellow oil. For **a**, $^{Cl}Fp(CH_2)_5CH_3$: ^1H NMR ($CDCl_3$): 4.59 ppm (s, 2H, $C_5\mathbf{H}_4$), 4.55 ppm (s, 2H, $C_5\mathbf{H}_4$), 3.55 ppm (t, 2H, $C\mathbf{H}_2Cl$), 2.40 ppm (t, 2H, $(C_5H_4)C\mathbf{H}_2$), 1.95 ppm (q, 2H, $CH_2C\mathbf{H}_2CH_2Cl$), 1.41 (m, 2H, $FeC\mathbf{H}_2$), 1.26 ppm (m, 8H, $CH_2(C\mathbf{H}_2)_4$), 0.87 ppm (m, 3H, $(CH_2)_5C\mathbf{H}_3$); Yield: 1.94 g (42%); For **b**, $^{Cl}Fp(CH_2)_4CH{=}CH_2$: ^1H NMR ($CDCl_3$): 5.80 ppm (ddt, J = 16.8 Hz, 10.2 Hz, 7.0 Hz, 1H, $C\mathbf{H}{=}CH_2$), 4.94 ppm (m, 2H, $CH{=}C\mathbf{H}_2$), 4.60 ppm (s, 2H, $C_5\mathbf{H}_4$), 4.56 ppm (s, 2H, $C_5\mathbf{H}_4$), 3.55 ppm (t, 2H, $C\mathbf{H}_2Cl$), 2.39 ppm (t, 2H, $(C_5H_4)C\mathbf{H}_2$), 2.00 ppm (m, 2H, $CH_2C\mathbf{H}_2CH_2Cl$), 1.42 ppm (m, 2H, $FeC\mathbf{H}_2$), 1.26 ppm (m, 6H, $CH_2(C\mathbf{H}_2)_3CH{=}CH_2$); Yield: 2.54 g (53%).

2.3.3 Synthesis of ^{P}FpR, $[\eta^5\text{-}(C_6H_5)_2P(CH_2)_3C_5H_4]Fe(CO)_2R$

In a Schlenk RB flask containing distilled THF (100 mL) and 1.0 eq of ^{Cl}FpR (**a**: 2.3 g, 6.8 mmol; **b**: 2.5 g, 7.4 mmol), 2.0 eq of $NaPPh_2$ solution (0.5 M in THF; **a**: 27.2 mL, 13.6 mmol; **b**: 29.7 mL, 14.9 mmol) were added dropwise into the solution at 0 °C, generating a bright red/orange solution. The reaction mixture was warmed to room temperature after the addition of $NaPPh_2$ and stirred for 2 hours. Degassed methanol (10 mL) was added to quench the excess $NaPPh_2$ after the reaction was completed. Afterwards, THF was removed under vacuum, and the crude product was re-dissolved in a small amount of hexane and passed through a column with a plug of Celite to remove NaCl salts. The crude product was further purified by silica-gel column chromatography using a mixture of hexane/DCM (3:1 v/v) as eluent. The first yellow band was collected and concentrated under vacuum, yielding a red-orange oil. For **a**, R = $(CH_2)_5CH_3$: ^{31}P NMR ($CDCl_3$): -15.8 ppm (coordinated phosphine); ^1H NMR ($CDCl_3$): 7.60-7.31 ppm (m, 10H, $P(C_6\mathbf{H_5})_2$) 4.56 ppm (s, 2H, $C_5\mathbf{H}_4$), 4.48 ppm (s, 2H, $C_5\mathbf{H}_4$), 2.33 ppm (t, 2H, $C\mathbf{H}_2PPh_2$), 2.06 ppm (t, 2H, $(C_5H_4)C\mathbf{H}_2$), 1.85 ppm (m, 2H, $CH_2C\mathbf{H}_2CH_2P$), 1.36 (2H, Fe-$C\mathbf{H}_2$) 1.25 ppm (8H, $FeCH_2(C\mathbf{H}_2)_4$),

0.86 ppm (3H, $(CH_2)_5CH_3$); Yield: 1.93 g (58%). For **b**, R = $(CH_2)_4CH=CH_2$: ^{31}P NMR ($CDCl_3$): -15.8 ppm (uncoordinated phosphine); ^1H NMR ($CDCl_3$): 7.35 ppm (m, 10H, C_6H_5), 5.81 ppm (ddt, J = 16.7 Hz, 9.0 Hz, 6.8 Hz, 1H, $CH=CH_2$), 4.94 ppm (m, 2H, $CH=CH_2$), 4.56 ppm (s, 2H, C_5H_4), 4.84 ppm (s, 2H, C_5H_4), 2.34 ppm (t, 2H, CH_2PPh_2), 2.05 ppm (t, 2H, $(C_5H_4)CH_2$), 1.63 ppm (m, 2H, $CH_2CH_2CH_2P$), 1.39 ppm (m, 2H, $FeCH_2$), 1.26 ppm (m, 6H, $CH_2(CH_2)_3CH=CH_2$); Yield: 2.26 g (63%).

2.4 Synthesis of P(^{P}FpR) Macrocycles

In a Schlenk flask containing ^{P}FpR (1 g, 2.05 mmol, 70 wt.% in THF), MIP was initiated by heating the reaction flask to 60 °C for 48 hours. After 48 hours, MIP was terminated by cooling the reaction flask to room temperature. The crude product was dissolved in a small amount of THF (5 mL) and precipitated into hexane (400 mL). The polymer was separated *via* filtration and washed with hexane 3 times to remove impurity traces. The precipitates were dried under vacuum for 24 hours, yielding yellow powders. For **a**, R = $(CH_2)_5CH_3$: ^{31}P NMR ($CDCl_3$): 72.4 ppm; ^1H NMR ($CDCl_3$): 7.38-7.25 ppm (br, 10H, C_6H_5), 4.08-3.95 ppm (m, 4H, C_5H_4), 2.76 ppm (s, 1H, $Fe(CO)CH_2(CH_2)_4$), 2.52 ppm (s, 1H, $Fe(CO)CH_2(CH_2)_4$), 2.24-2.12 ppm (m, 4H, $CH_2CH_2CH_2PPh_2$), 1.25-1.05 ppm (br, 10H, $CH_2CH_2CH_2PPh_2$ and $Fe(CO)CH_2(CH_2)_4CH_3$), 0.83 ppm (s, 3H, $Fe(CO)CH_2(CH_2)_4CH_3$). Yield: 730 mg (73%); For **b**, R = $(CH_2)_4CH=CH_2$: ^{31}P NMR ($CDCl_3$): 72.3 ppm. ^1H NMR ($CDCl_3$): 7.45-7.25 ppm (br, 10H, C_6H_5), 5.73 ppm (m, 1H, $(CH_2)_4CH=CH_2$), 4.90 ppm (m, 2H, $(CH_2)_4CH=CH_2$), 4.09-3.95 ppm (m, 4H, C_5H_4), 2.78 ppm (s, 1H, $Fe(CO)CH_2(CH_2)_3CH=CH_2$), 2.53 ppm (s, 1H, $Fe(CO)CH_2(CH_2)_3CH=CH_2$), 2.25-2.11 ppm (m, 4H, $CH_2CH_2CH_2PPh_2$), 1.92 ppm (m, 2H, $CH_2CH_2CH_2PPh_2$), 1.45-1.18 ppm (m, 6H, $Fe(CO)CH_2(CH_2)_3CH=CH_2$). Yield: 760 mg (76%).

2.5 Synthesis of Cyclic ^{P}FpR Small Rings

A distilled THF solution (60 mL) of ^{P}FpR (600 mg, 1.23 mmol, 1.0 wt.% in THF) was stirred in a Schlenk flask at 60 °C for 48 hours. After 48 hours, the resulting solution was cooled to room temperature, and THF was removed under vacuum. The crude product was purified by silica gel chromatography using a hexane/DCM (3:1 v/v) mixture as eluent. The first orange band was collected, yielding a bright orange oil. For **a**, R = $(CH_2)_5CH_3$: ^{31}P NMR (300 MHz, $CDCl_3$): 71.6 ppm; ^{1}H NMR (300 MHz, $CDCl_3$): 7.61 ppm (s, 2H, $C_6\mathbf{H}_5$), 7.39 ppm (s, 3H, $C_6\mathbf{H}_5$), 7.16 ppm (m, 5H, $C_6\mathbf{H}_5$), 4.68 ppm (s, 1H, $C_5\mathbf{H}_4$), 4.60 ppm (s, 1H, $C_5\mathbf{H}_4$), 4.24 ppm (s, 1H, $C_5\mathbf{H}_4$), 3.94 ppm (s, 1H, $C_5\mathbf{H}_4$), 2.78 ppm (tdd, *J*=13.6 Hz, 6.8 Hz, 2.3 Hz, 1H, $CH_2C\mathbf{H}_2P$), 2.54 ppm (m, 3H), 2.37 ppm (m, 1H), 2.17 ppm (m, 1H), 1.99 ppm (m, 1H), 1.40 ppm (m, 1H), 1.14 ppm (m, 3H), 1.02 ppm (m, 3H), 0.86 ppm (m, 2H), 0.79 ppm (m, 3H, $CH_2C\mathbf{H}_3$);^{13}C NMR (300 MHz, $CDCl_3$): 279.58 ppm (d, *J* = 28.11 Hz), 220.46 ppm (d, *J* = 28.11 Hz), 138.16 ppm (d, *J* = 49.20 Hz), 136.42 ppm (d, *J* = 38.65 Hz), 133.69 ppm (s), 133.53 ppm (s), 130.95 ppm (s), 130.84 ppm (s), 130.05 ppm (s), 128.64 ppm (s), 128.34 ppm (s), 128.17 ppm (s), 127.90 ppm (s), 127.77 ppm (s), 99.25 ppm (s), 91.65 ppm (s), 82.20 ppm (s), 81.77 ppm (s), 73.12 ppm (s), 65.81 ppm (d, *J* = 5.27 Hz), 31.74 ppm (s), 28.77 ppm (s), 24.90 ppm (s), 24.68 ppm (s), 22.53 ppm (s), 21.13 ppm (s), 18.50 ppm (d, *J* = 29.8 Hz), 14.08 ppm (s); FT-IR: 1906 cm^{-1} (terminal CO) and 1596 cm^{-1} (acyl CO), ESI-MS: *m/z* = 488.16, calculated for $C_{28}H_{33}FeO_2P$: 488.38; Anal. Calculated for $C_{28}H_{33}FeO_2P$: C 68.86, H 6.81; found: C 68.76, H 6.86. Yield: 500 mg (83%); For **b**, R = $(CH_2)_4CH{=}CH_2$: ^{31}P NMR (300 MHz, $CDCl_3$): 71.5 ppm (s); ^{1}H NMR (300 MHz, $CDCl_3$): 7.62 ppm (m, 2H, C_6H_5), 7.39 ppm (m, 3H, C_6H_5), 7.16 ppm (m, 5H, C_6H_5), 5.69 ppm (ddt, J=17.3 Hz, 10.2 Hz, and 6.5 Hz, 1H, H_2C-C**H**=CH_2), 4.86 ppm (m, 2H, -CH=C$\mathbf{H}_2$), 4.69 ppm (s, 1H, C_5H_4), 4.60 ppm (s, 1H, C_5H_4), 4.23 ppm (s, 1H, C_5H_4), 3.94 ppm (s, 1H, C_5H_4), 2.77 ppm (tdd, J=13.6

Hz, 6.7 Hz, 2.1 Hz, 1H, $CH_2C\mathbf{H}_2P$), 2.55 ppm (m, 3H), 2.38 ppm (m, 1H), 2.16 ppm (m, 1H), 2.01ppm (m, 1H), 1.82 ppm (m, 2H), 1.40 ppm (m, 1H), 1.16 ppm (m, 1H), 0.96 ppm (m, 3H); ^{13}C NMR (300 MHz, $CDCl_3$): 279.42 ppm (d, J = 25.22 Hz), 220.41 ppm (d, J = 28.31 Hz), 139.23 ppm (s), 138.08 ppm (d, J = 46.64 Hz), 136.23 ppm (d, J = 38.87 Hz), 133.64 ppm (s), 133.51 ppm (s), 130.94 ppm (s), 130.82 ppm (s), 130.07 ppm (s), 128.68 ppm (s) 128.30 ppm (s), 128.18 ppm (s), 127.92 ppm (s), 127.80 ppm (s), 113.94 ppm (s), 99.25 ppm (s), 91.70 ppm (s), 82.19 ppm (s), 81.78 ppm (s), 73.12 ppm (s), 65.47 ppm (d, J =5.5 Hz), 33.71 ppm (s), 28.41 ppm (s), 24.68 ppm (s), 24.51 ppm (s), 21.10 ppm (s), 18.48 ppm (d, J = 26.43 Hz); FT-IR: 1908 cm^{-1} (terminal CO) and 1599 cm^{-1} (acyl CO); ESI-MS: m/z = 486.15, calculated for $C_{28}H_{31}FeO_2P$ **(3b):** 486.36; Anal. Calculated for $C_{28}H_{31}FeO_2P$: C 69.15, H 6.42; found: 62.86, H 6.62. Yield: 480 mg (80%).

3.0 Results and Discussion

MIP of ^{P}FpR was initially carried out in bulk at 105 °C for 48 hours, as described in literature.[43] The oil-like monomer gradually became viscous after 1 hour of polymerization, which was indicated by the immobility of the stir bar inside the Schlenk flask. After 48 hours, the polymerization was terminated by cooling the Schlenk flask to room temperature. A sample of the crude product was dissolved in $CDCl_3$ and analyzed by ^{31}P (Figure 3.1) and ^{1}H NMR (Figure 3.2a) spectroscopies.

As shown in Figure 3.1, the crude product shows two chemical shifts at 72 ppm and 71 ppm, which correspond to the formation of two Fe-P coordination bonds as a result of MIRs.[40-43] The MIP crude products were separated by precipitation in hexane followed by filtration. The P(^{P}FpR) macromolecules were isolated as the precipitate, and showed one signal at 72 ppm in the ^{31}P NMR spectrum (Figure 3.1b). This macromolecule adopts a cyclic structure due to the non-linear, piano-stool coordination geometry and the presence of Fe-Cp bonds in the backbone of P(^{P}FpR).[41,43] On the other hand, the hexane-soluble unknown side product was collected from the filtrate, which shows one signal at 71 ppm in the corresponding ^{31}P NMR spectrum (Figure 3.1b). The chemical structure for this product needs to be characterized.

Similar peak separation was also observed in the Cp region from 3.8-4.8 ppm in the corresponding ^{1}H NMR spectra (Figure 3.2). One Cp signal was observed in the P(^{P}FpR) precipitate (Figure 3.2b), confirming the cyclic topology of P(^{P}FpR) due to the absence of end group signals. The spectrum of the hexane-soluble side product in the filtrate shows four Cp signals, suggesting the formation of four chemically different Cp protons. A more detailed peak assignment for this unknown product will be discussed in Section 3.2.2.

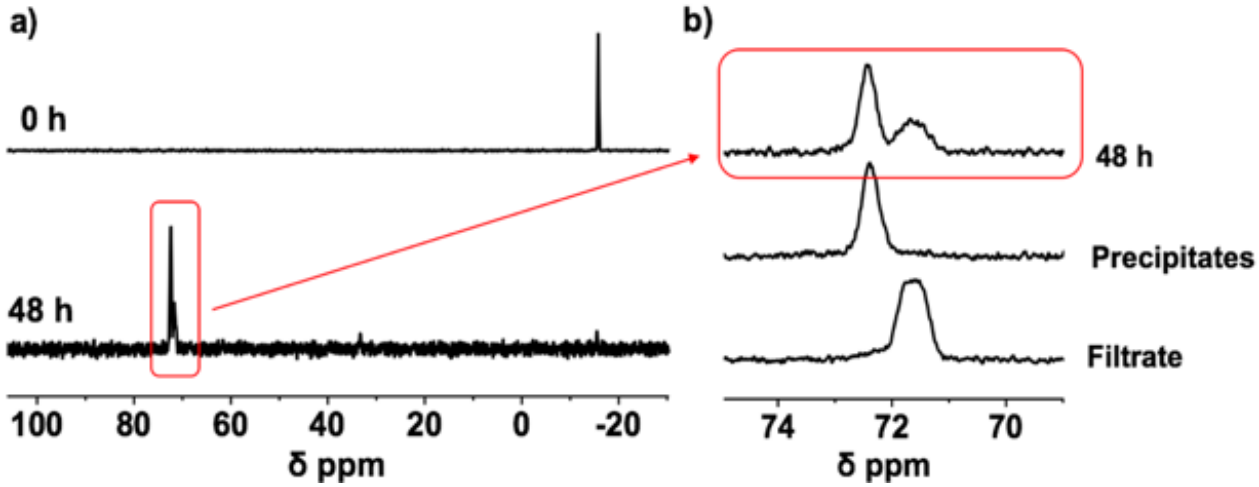

Figure 3.1: a) ^{31}P NMR ($CDCl_3$) spectra before and after MIP, b) ^{31}P NMR ($CDCl_3$) spectra for the separated products.

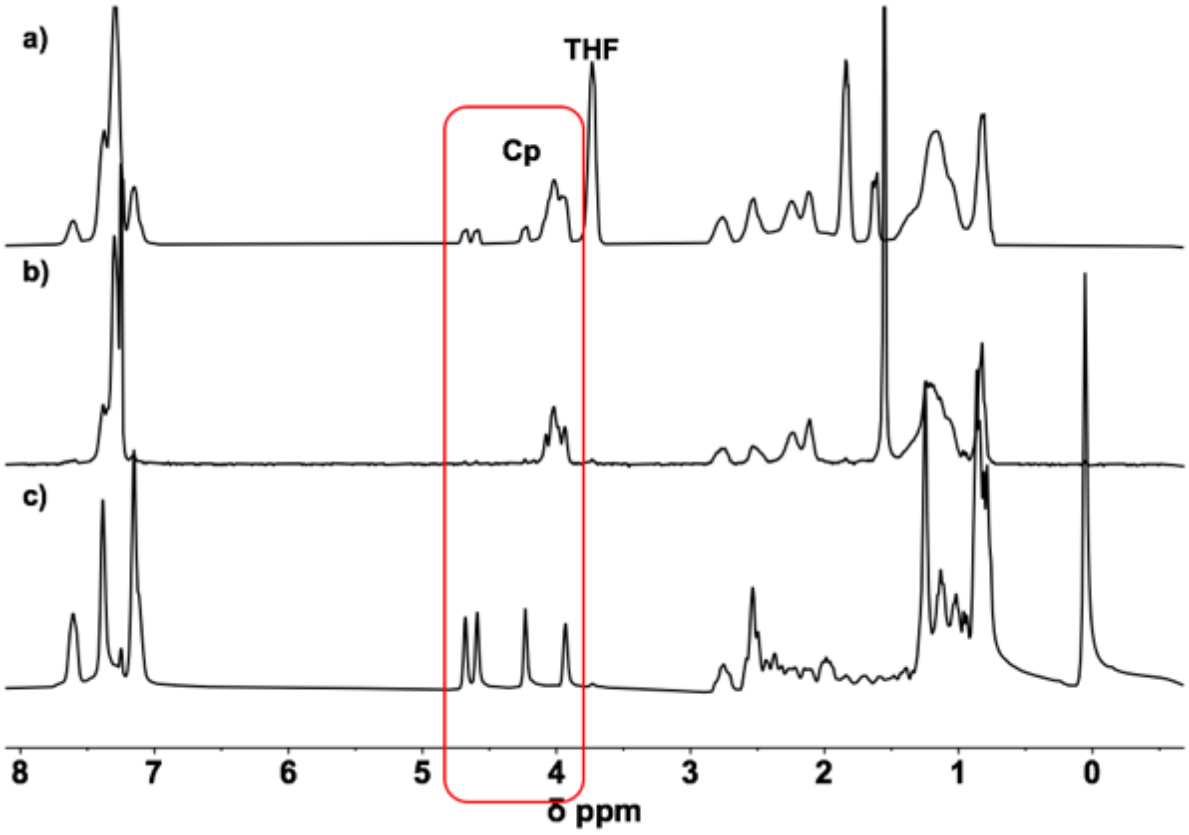

Figure 3.2: ^{1}H NMR ($CDCl_3$) spectra for a) MIP crude products, b) P(^{P}FpR) precipitate, and c) filtrate prepared by MIP in bulk at 105 °C.

3.1 P(^{P}FpR) Macrocycle Characterization

3.1.1 End Group Analysis by NMR

To confirm the cyclic structure of P(^{P}FpR) macromolecules, a linear P(FpP) was synthesized for comparison (Figure 3.3a), as described in the literature.[41] Linear and cyclic macromolecules differ with the presence or absence of end groups. ^{1}H and ^{31}P NMR spectroscopies were performed as complementary techniques for the end group analysis. As seen in the ^{1}H NMR spectra, the linear P(FpP) exhibits a broad signal at 4.3 ppm due to the Cp groups in the main-chain, and a small signal at 4.7 ppm due to the Cp ring in the unreacted Fp end group (Figure 3.3a). In the case of P(^{P}FpR), only one broad Cp signal at 4.0 ppm was observed (Figure 3.3b). Similarly, the ^{31}P NMR spectrum for linear P(FpP) shows an end group signal for oxidized phosphorus (P=O bond) at 33 ppm, aside from the major peak at 73 ppm which represents the Fe-P bonds in the polymer backbone (Figure 3.3a). The P(^{P}FpR) macromolecules reveal only one signal at 72 ppm (Figure 3.3b). The absence of end group signals in P(^{P}FpR) suggests the cyclic structure of the macromolecules.

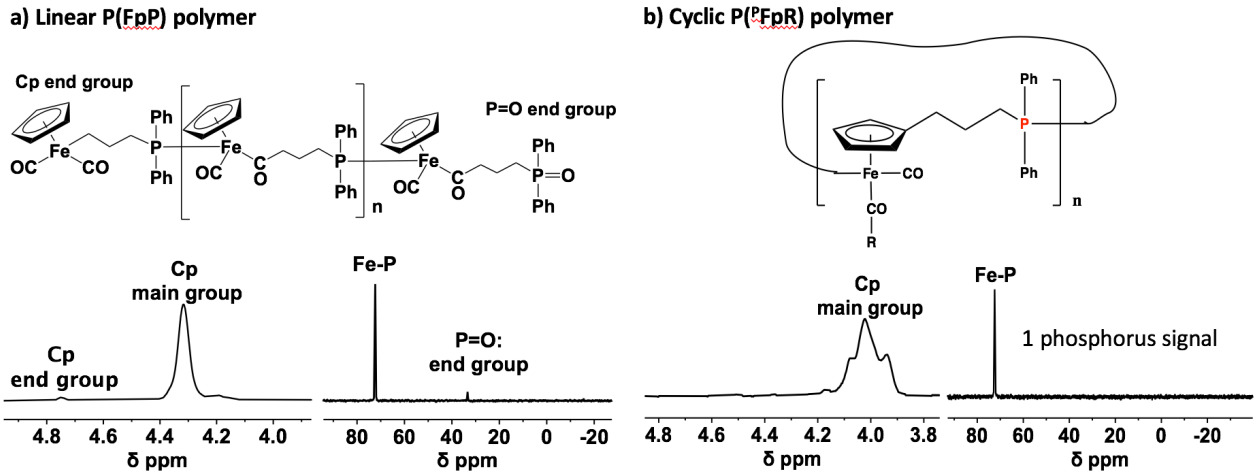

Figure 3.3: End group analysis of a) linear P(FpP) polymer, and b) cyclic P(^{P}FpR) polymer.

3.1.2. Cyclic Topology by TEM Analysis

To further confirm the structure of P(^{P}FpR) macromolecules, TEM analysis was performed. The TEM samples were prepared by adding a drop of P(^{P}FpR) in THF solution (5 mg/mL) on a copper grid substrate. As seen in Figure 3.4, some ring-like morphologies with white centers of *ca.* 20-30 nm in diameters were observed. This contrast was caused by the breakage of the carbon substrate after exposing the grid to the electron beam for a few minutes.[43] By comparing the circumference and the size of the monomer, the DP for the macrocycles was estimated to range from 40 to 60 repeating units. The absolute M_w of the sample, as measured by GPC (using the triple detectors) was *ca*. 23,000 g/mol with a PDI value of 1.5, corresponding to a DP of 49, which matches the value estimated from the TEM image. The broad MW distribution suggests that non-uniformed rings of different sizes were produced during MIP, which is evident in the TEM image with the presence of smaller rings in the background. The GPC elution trace also shows tailing towards the low MW end, which is in good agreement with the high PDI value.

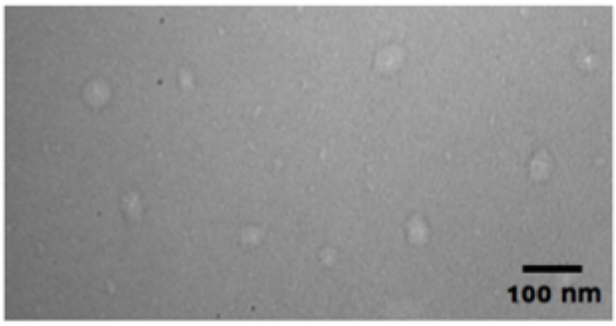

Figure 3.4: TEM image for P(^{P}FpR) macrocycles. Scale bar is 100 nm.

3.1.3 Molecular Weight by MALDI-TOF Analysis

MALDI-TOF analysis of the polymers was attempted, with and without matrix, to measure the absolute MW of P(^{P}FpR). The matrices were prepared at *ca.* 10-40 mg/mL in appropriate solvents, as summarized in Table 3.1. There are many factors that can affect the ionization of polymer samples including sample concentration, solvent polarity, and the matrix system. A suitable matrix eases the ionization process, which allows the polymers to be ionized for measurement. According to literature reviews, ferrocene-based oligomers could be ionized and detected in MALDI-TOF MS using dithranol as matrix.[32] As a result, dithranol was selected as the first matrix for MALDI-TOF experiment for MW measurements of P(^{P}FpR). DCTB (Table 3), which allows lower energy ionization than dithranol, has also been reported as a matrix for metallo-macrocycles.[44] Other polar matrices, as listed in Table 3, were also tested with the P(^{P}FpR) macrocycles. However, none of these matrices provided polymer signals, aside from the signal from the matrix. A cation source, from silver trifluoroacetate, was also added in the dithranol and DCTB matrix systems to ease the ionization process, but no meaningful results were obtained. This technique for the characterization of P(^{P}FpR) macrocycles remains to be a matter of future research.

Table 3.1: MALDI-TOF experiments with different matrices.

Matrix	Chemical structure	Concentration (solvent)	Signals
9AA	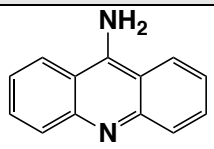	25 mg/mL (THF)	X
DIT	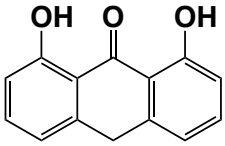	40 mg/mL (THF)	X
DCTB	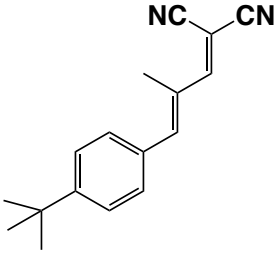	40 mg/mL (THF)	X
DHB	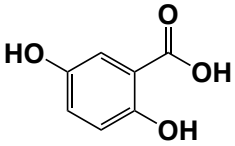	25 mg/mL (1:1 ACN/H_2O + 0.1% TFA)	X
HCCA	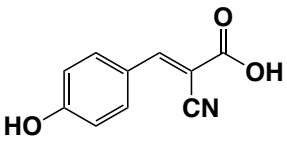	10 mg/mL (1:1 ACN/H_2O + 0.1% TFA)	X
HPA	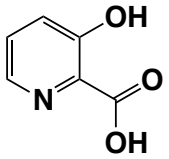	10 mg/mL (1:1 ACN/H_2O + 0.1% TFA)	X
SA	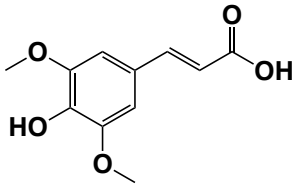	10 mg/mL (1:1 ACN/H_2O + 0.1% TFA)	X

3.1.4 Molecular Weight by GPC Analysis

GPC measurements on P(^{P}FpR) macrocycles were also carried out to determine their MW. The measurements were first attempted on a GPC instrument equipped with triple detectors, which can determine the absolute MW of the samples from light scattering. The preliminary results showed that the M_n of the P(^{P}FpR) macrocycles (prepared by MIP in 50 wt.% THF) was *ca.* 23,000 g/mol, with a PDI value of 1.5. However, due to some technical difficulties, other GPC instrumentation was used for the measurements instead. A typical GPC elution curve is presented in Figure 3.5. As seen in the figure, a broad peak is observed between 1300-1400 seconds, corresponding to the elution of P(^{P}FpR). The other sharp peak at 1450-1500 seconds represents the LiBr salt in DMF solvent. Since there was overlap between the elution time of the polymer and the solvent, only the peak MW (M_p) was determined and reported as a relative MW calculated from PS standards. The GPC results show that the M_p of the P(^{P}FpR) macrocycle, prepared by MIP in 50 wt.% THF, was *ca.* 18,000 g/mol, corresponding to a DP of 36 repeating units. Although these M_p values cannot represent the absolute MW of the polymers, they seem to be in good agreement with the absolute MW determined before. As a result, these M_p values were used as a reference to compare the relative size of the polymers prepared under different conditions, which will be discussed in details in Section 3.3.3.

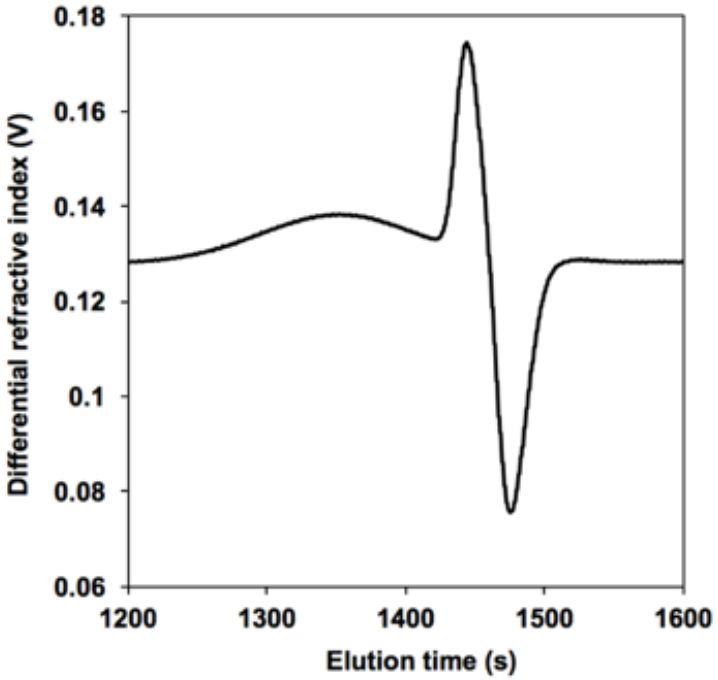

Figure 3.5 GPC elution curve for P(^{P}FpR) macrocycles.

3.2 Small Molecules Characterization

The hexane-soluble unknown side product isolated in the filtrate was further analyzed. The products were characterized by X-ray crystallography, NMR spectroscopy, FT-IR spectroscopy, ESI-MS, and elemental analysis.

3.2.1 X-ray Crystallography

Yellow crystals of the unknown side product were obtained from a saturated hexane solution upon a slow solvent evaporation. X-ray crystallographic analysis of the crystals was subsequently conducted, and their chemical structures and crystallographic data are revealed in Figure 3.6 and Table 3.2. Both molecules crystalized in a monoclinic system with a $P2_1/c$ space group. The hexane-soluble unknown product is a cyclized ^{P}FpR monomer, which consists of a Fe-P coordination bond, as a result of the intramolecular migratory insertion cyclization (MIC), as proposed in Scheme 3.1.

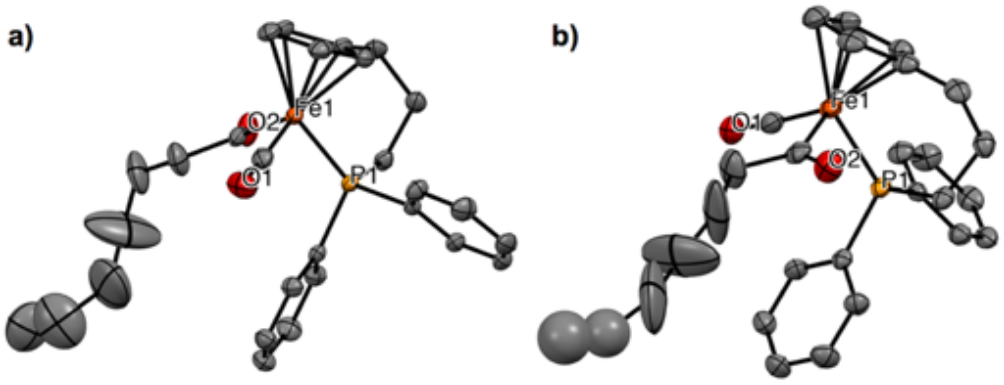

Figure 3.6: ORTEP (Oak Ridge Thermal Ellipsoid Plot) drawings (30% probability ellipsoids) for the molecular structures of cyclic ^{P}FpR, for R = a) $(CH_2)_5CH_3$ and b) $(CH_2)_4CH{=}CH_2$. Hydrogen atoms are omitted for clarity.

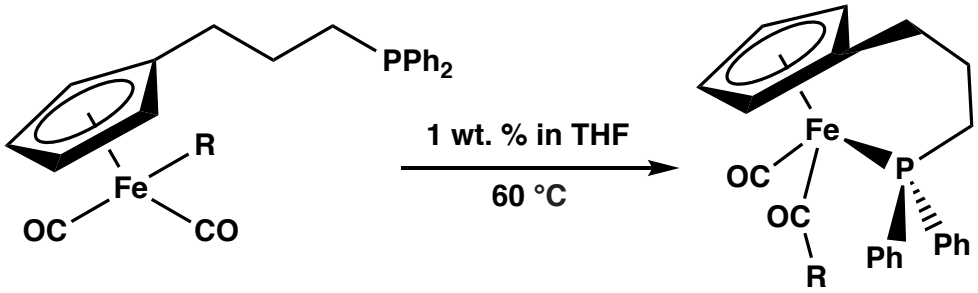

Scheme 3.1 Intramolecular migratory insertion cyclization (MIC) of ^{P}FpR.

Table 3.2: Summary of crystallographic data for cyclized ^{P}FpR.

Compound	^{P}FpR, R = $(CH_2)_5CH_3$	^{P}FpR, R = $(CH_2)_4CH{=}CH_2$
Empirical formula	$C_{28}H_{33}FeO_2P$	$C_{28}H_{31}FeO_2P$
Formula weight	488.36	486.35
Temperature/K	200(2)	200(2)
Crystal system	monoclinic	monoclinic
Space group	$P2_1/c$	$P2_1/c$
a, Å	8.9432(9)	8.8180(5)
b, Å	25.316(2)	25.3531(15)
c, Å	10.9549(10)	10.9132(7)
α, °	90	90
β, °	97.408(3)	95.8368(16)
γ, °	90	90
Volume, $Å^3$	2459.5(4)	2427.1(3)
Z	4	4
$\rho_{calc,}$ g/cm^3	1.319	1.331
μ, mm^{-1}	0.701	0.710
F(000)	1032.0	1024.0
Crystal size/mm^3	0.200 × 0.100 × 0.020	0.200 × 0.100 × 0.080
Radiation	MoKα (λ = 0.71073)	MoKα (λ = 0.71073)
2Θ range for data collection/°	4.08 to 55.996	4.644 to 51.994
Index ranges	$-11 \le h \le 11$, $-27 \le k \le 33$, $-14 \le l \le 14$	$-10 \le h \le 10$, $-31 \le k \le 31$, $-13 \le l \le 12$
Reflections collected	27202	26325
Independent reflections	5944 [R_{int} = 0.0444, R_{sigma} = 0.0394]	4762 [R_{int} = 0.0435, R_{sigma} = 0.0295]
Data/restraints/parameters	5944/4/290	4762/0/280
Goodness-of-fit on F^2	1.233	1.171
Final R indexes [I>=2σ (I)]	R_1 = 0.0506, wR_2 = 0.0978	R_1 = 0.0922, wR_2 = 0.1943
Final R indexes [all data]	R_1 = 0.0784, wR_2 = 0.1058	R_1 = 0.1119, wR_2 = 0.2037
Largest diff. peak/hole / e $Å^{-3}$	0.66/-0.55	0.82/-0.89

3.2.2 NMR characterization

The cyclized ^{P}FpR monomer was further characterized by ^{1}H, ^{13}C, COSY, and HMQC NMR spectroscopy.

As shown in Figure 3.7, the ^{1}H NMR spectrum for the cyclic ^{P}FpR, for R = $(CH_2)_4CH{=}CH_2$, revealed 3 signals from 7.16-7.62 ppm and 4 signals from 3.8-4.8 ppm, which were assigned to the protons on the two phenyl groups and the Cp ring, respectively. Four Cp proton signals were observed, indicating their different chemical environments. These signals were due to the presence of the Fe stereocenter as a result of the formation of a chiral chelate ring.[11,14] The chemical shifts at 5.68 ppm and 4.86 ppm, with a proton integration ratio of 1 : 2, represent the vinyl protons H_h and H_i respectively.

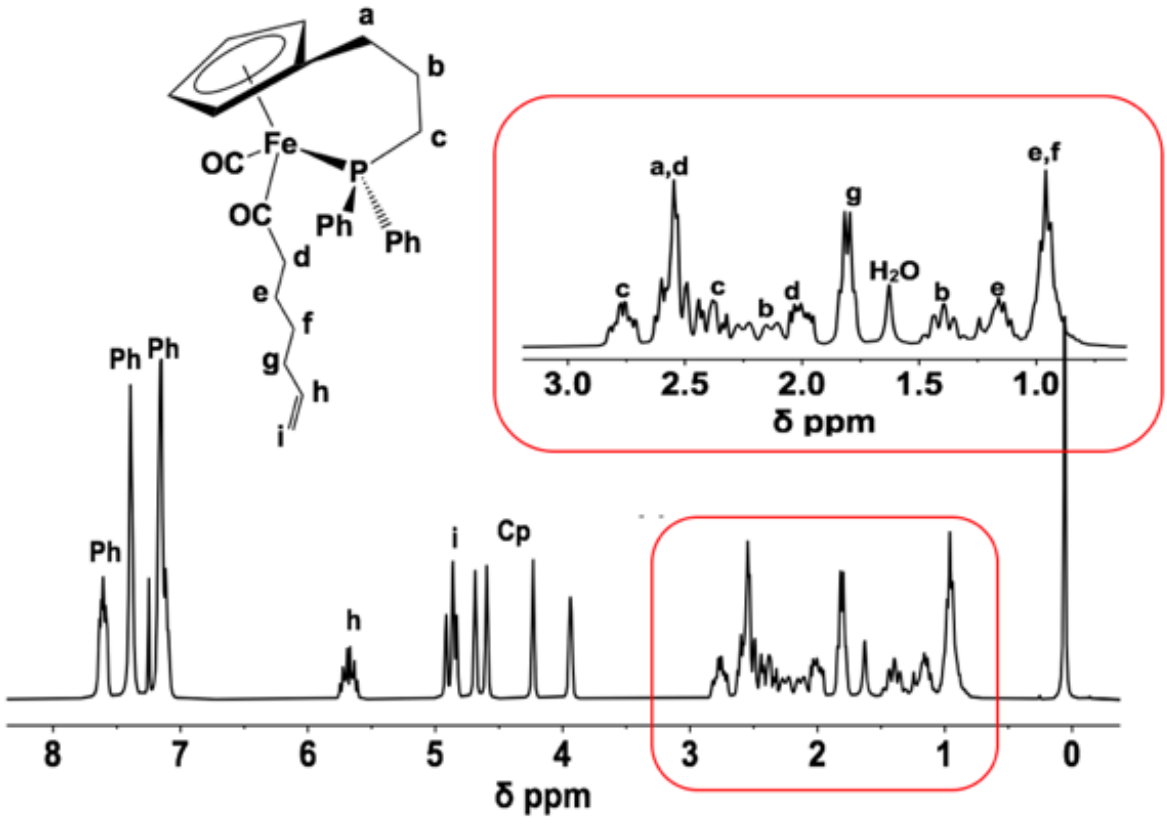

Figure 3.7: ^{1}H NMR ($CDCl_3$) spectrum for cyclic ^{P}FpR, for R = $(CH_2)_4CH{=}CH_2$.

In the corresponding ^{13}C NMR spectrum, as shown in Figure 3.8, the peaks at 73.1-99.3 ppm, 127.8-138.1 ppm, 220 ppm, and 280 ppm were assigned to the 5 Cp carbons, 12 phenyl carbons, the terminal CO carbon, and the acyl carbon, respectively. The appearance of the acyl CO group signal at 280 ppm confirmed the occurrence of migration as a result of MIC. The signal at 65.5 ppm was assigned to the α carbon (C_d) next to the electron withdrawing acyl CO group, which causes the chemical signal of C_d to appear at the lower field than the other CH_2 carbons. The carbon signals for the vinyl group, C_h and C_i, were observed at 139.2 ppm and 113.9 ppm, respectively. The chemical shift at 18.5 ppm was split into a doublet, which was assigned to C_c due to the P-C coupling with its neighboring phosphorus atom.

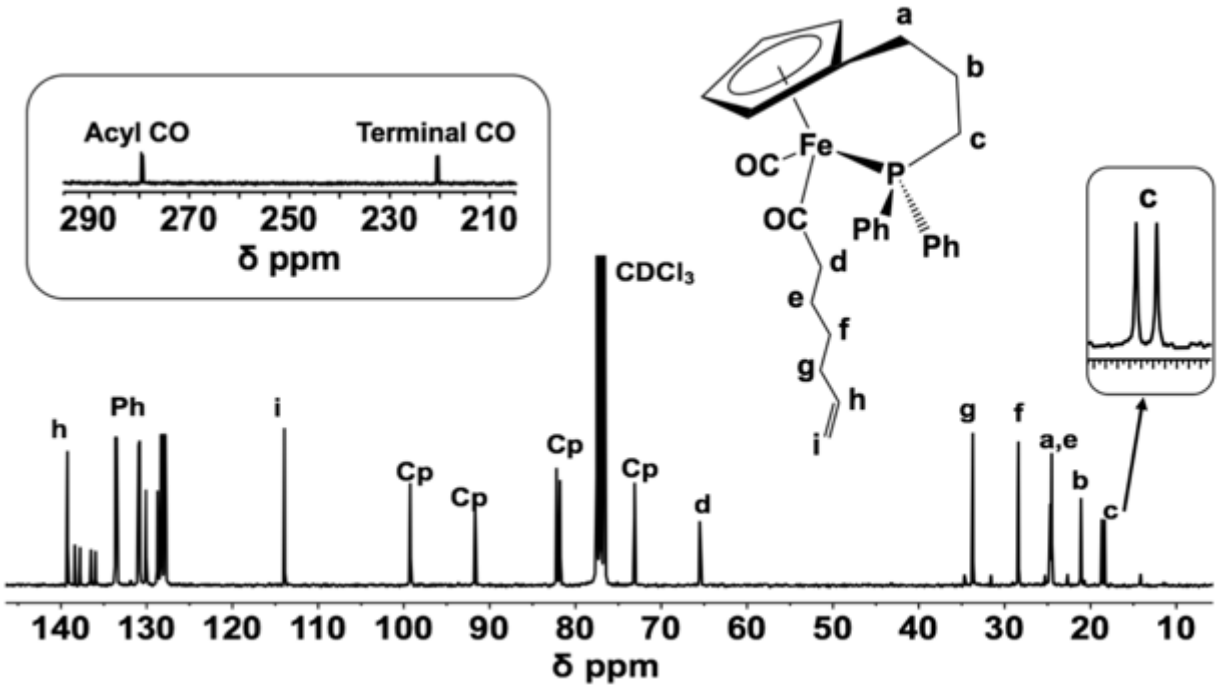

Figure 3.8: ^{13}C NMR ($CDCl_3$) spectrum for cyclic ^{P}FpR, for R = $(CH_2)_4CH{=}CH_2$.

Other protons (a-i) and carbons (a-i) peaks were also assigned and confirmed by ^{1}H-^{1}H COSY (correlation spectroscopy, Figure 3.9) and ^{13}C-^{1}H HMQC (heteronuclear multiple quantum correlation, Figure 3.10) 2D NMR experiments.

From the COSY spectrum in Figure 3.9, the known proton H_h at 5.68 ppm showed a coupling signal at 1.81 ppm, which was assigned to the neighboring protons H_g. Other proton couplings were also observed between H_g-H_f (1.81 ppm, 0.96 ppm) , H_f-H_e (0.96 ppm, 1.16 ppm), and H_e-H_d (1.16 ppm, 2.01 ppm and 2.55 ppm), which allowed the assignment of the rest of the protons on the hexyl chain. Due to the formation of the chiral bridged chelate ring and the presence of the Fe stereocenter, multiple sets of diastereotopic protons (b-e) are expected. The known carbon at 65 ppm, adjacent to the acyl carbon, also showed two coupling protons at 2.01 ppm and 2.55 ppm in the HMQC spectrum in Figure 3.10, representing the two diastereotopic protons, H_d. The rest of the carbons on the hexyl chain were assigned according to the C-H coupling signals observed in the HMQC spectrum. Protons H_g, H_f, and H_e show coupling signals with the carbons at 33.7 ppm, 28.4 ppm, and 24.5 ppm respectively.

The diastereotopic protons H_b and H_c showed 4 protons coupling signals (1.40 ppm, 2.16 ppm, 2.38 ppm and 2.77 ppm) with each other on the COSY spectrum (Figure 3.9), which are coupled to only 2 carbons at 21.1 ppm (C_b) and 18.5 ppm (C_c) respectively, as observed in the HMQC spectrum (Figure 3.10). C_b shows two coupling signals at 1.40 ppm and 2.16 ppm, which were assigned to the H_b diastereotopic protons. Protons at 2.38 ppm and 2.77 ppm were therefore assigned to H_c, which also show C-H coupling signals with C_c at 18.5 ppm. The remaining protons at 2.55 ppm and carbon at 24.7 ppm were assigned to H_a and C_a, which also show coupling signals on the HMQC spectrum. The cyclic ^{P}FpR, with R = $(CH_2)_5CH_3$, was also fully characterized in the same manner as discussed, in Appendix A1.

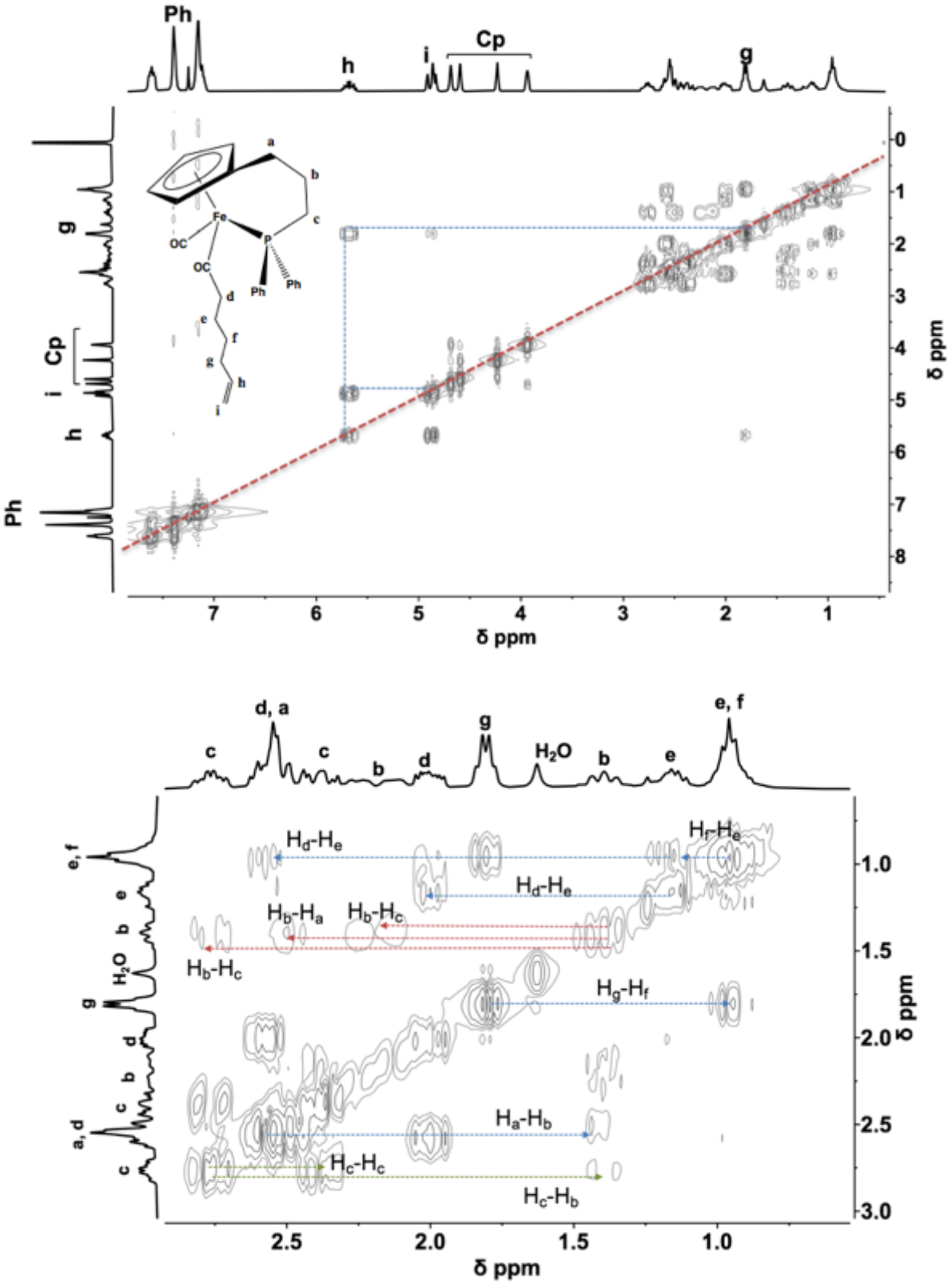

Figure 3.9: COSY (^{1}H-^{1}H) 2D NMR spectrum for cyclic ^{P}FpR, for R = $(CH_2)_4CH{=}CH_2$.

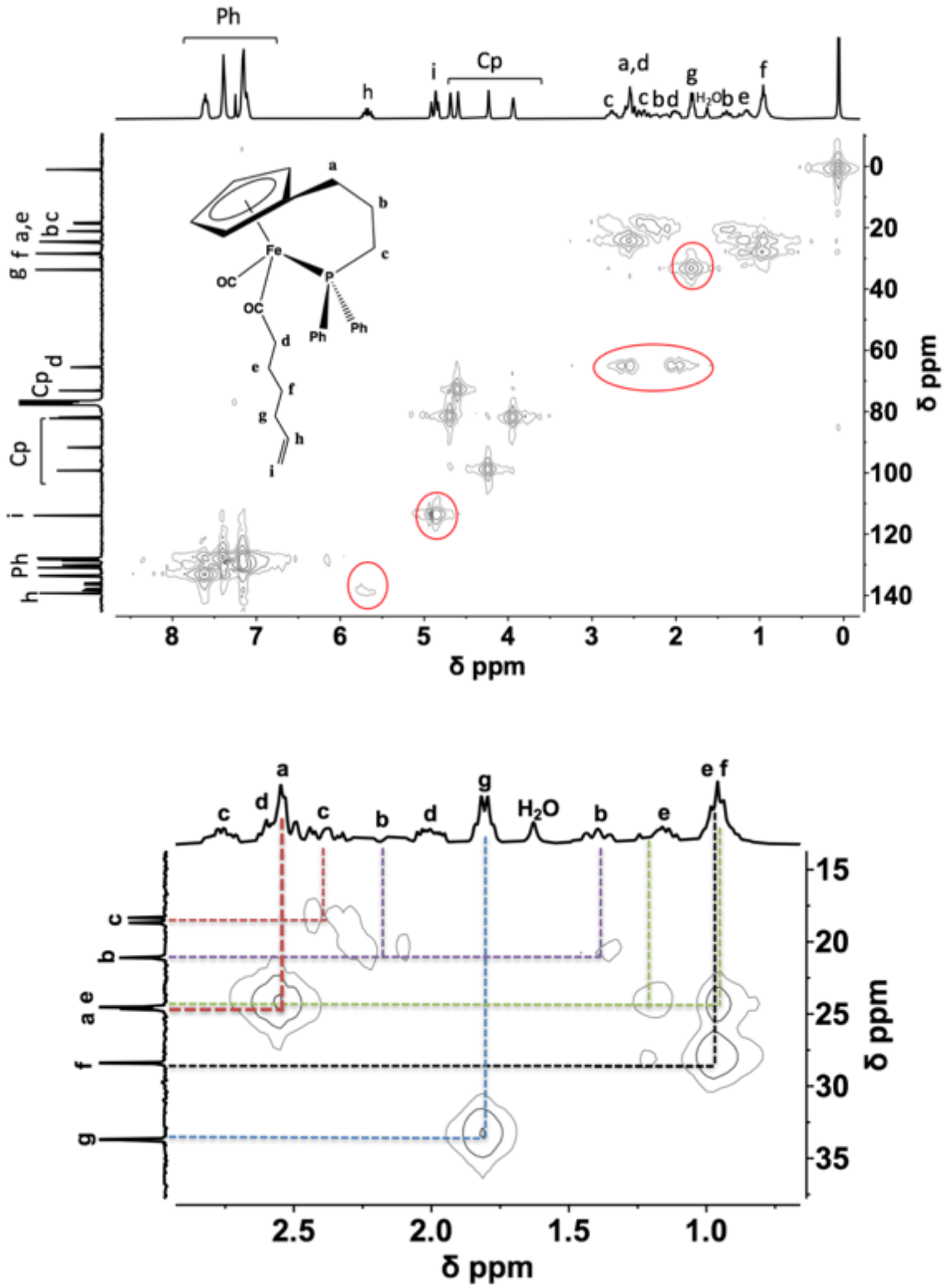

Figure 3.10: HMQC (^{13}C-^{1}H) 2D NMR spectrum for cyclic ^{P}FpR, for R = $(CH_2)_4CH{=}CH_2$.

3.2.3 Other Characterization

The occurrence of MIR was also confirmed by FT-IR spectroscopy. As seen in Figure 3.11, a new absorption signal at 1599 cm^{-1} appeared in the FT-IR spectrum, which indicated the formation of an acyl CO group as a result of intramolecular MIC. Elemental analyses was also performed, and the results also showed good agreement with the theoretical values of C and H, as presented in Table 3.3. The ESI-MS spectra had a molecular ion (MH^+) peak at 489.16 m/z for R= $(CH_2)_5CH_3$, and at 487.15 m/z for R = $(CH_2)_4CH{=}CH_2$, which match with their calculated theoretical MW of 488.38 g/mol and 486.37 g/mol, respectively (Figure 3.12). The observed base peak at 403.05 m/z corresponds to the Fp complex without the R groups.

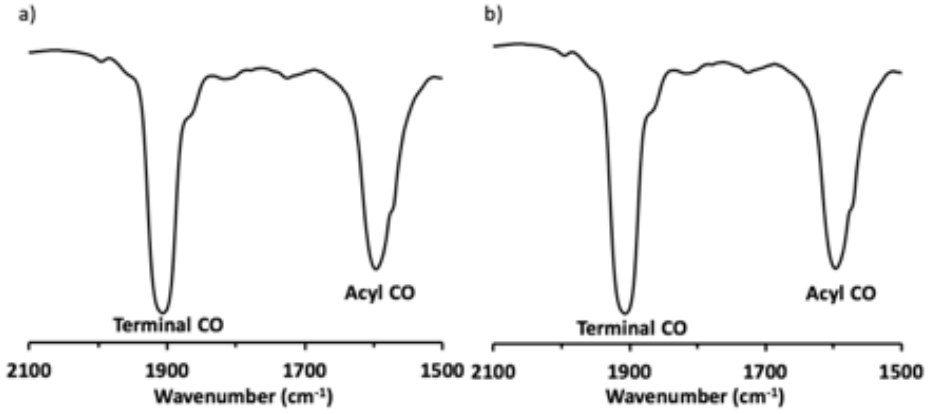

Figure 3.11: FT-IR spectra for cyclic ^{P}FpR, for R = a) $(CH_2)_5CH_3$, and b) $(CH_2)_4CH{=}CH_2$.

Table 3.3: Elemental analysis results for cyclic ^{P}FpR. Chemical formula for a) $C_{28}H_{33}FeO_2P$; b) $C_{28}H_{31}FeO_2P$.

R group	%	C	H
a) $(CH_2)_5CH_3$	Theoretical	68.86	6.81
	Experimental	68.76	6.86
b) $(CH_2)_4CH{=}CH_2$	Theoretical	69.15	6.42
	Experimental	62.86	6.62

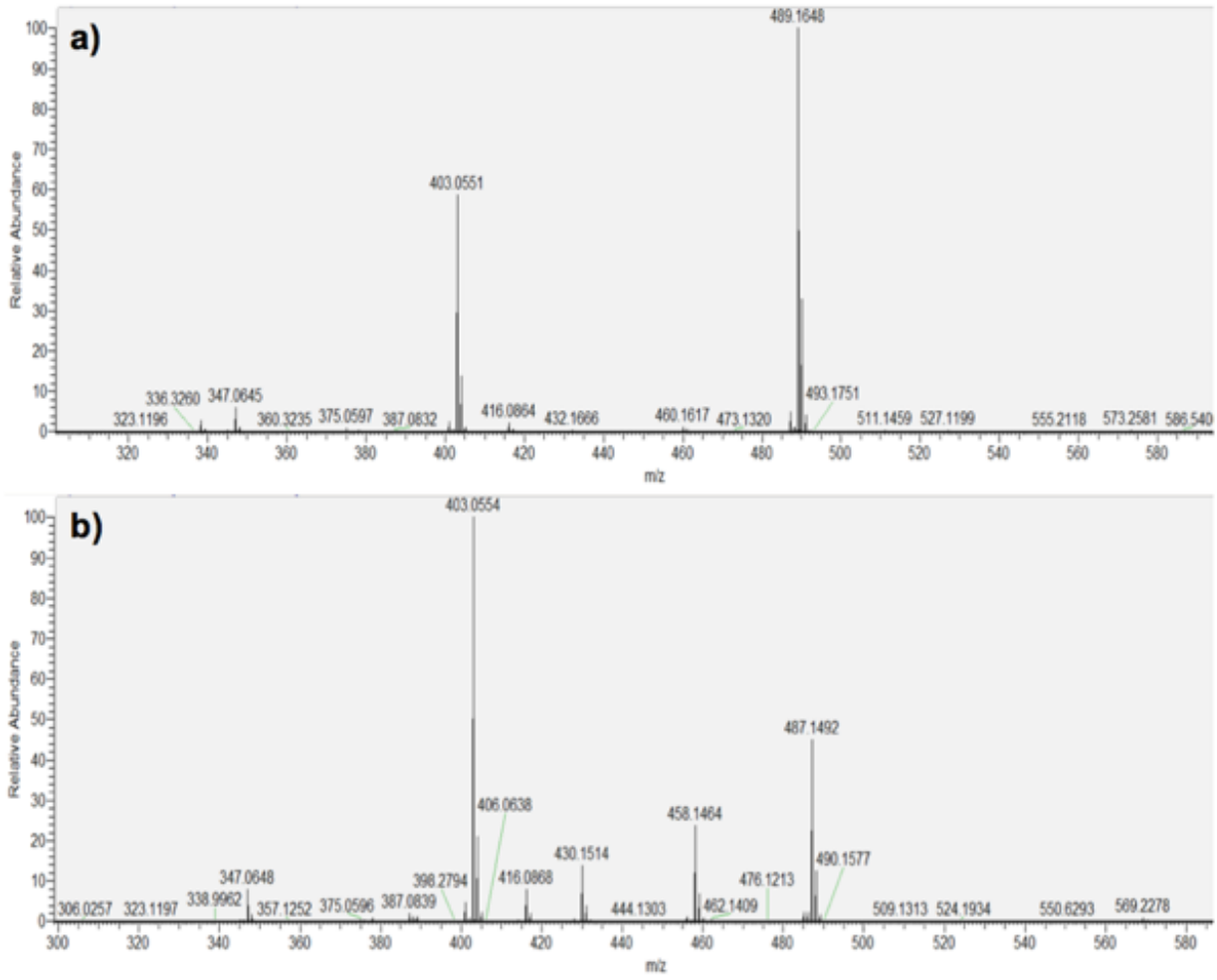

Figure 3.12: ESI-MS spectra for cyclic ^{P}FpR, for R = a) $(CH_2)_5CH_3$, and b) $(CH_2)_4CH{=}CH_2$.

3.3 Polymerization Condition Effects on MIR

The influence of the MIR conditions was examined to identify the most effective reaction routes to exclusively synthesize P(^{P}FpR) macrocycles or cyclic ^{P}FpR in maximum yield. As a result, MIP experiments were designed by varying the solvent system, temperature, and monomer concentration.

3.3.1 Solvent and temperature effects on MIP

The effect of the solvent on the MIP of ^{P}FpR, for R = $(CH_2)_5CH_3$, was investigated by performing the reaction in solution (50 % by weight) at 60 °C. After 48 hours, a sample of crude

product was dissolved in $CDCl_3$ and analyzed by ^{31}P NMR spectroscopy. As shown in Figure 3.13, when the polar solvent DMSO and DMF were used, the ^{31}P NMR spectra of the crude products showed a significant signal at 71 ppm, aside from the polymer peak at 72 ppm, representing the cyclized ^{P}FpR. In contrast, the THF system produced less cyclized ^{P}FpR, as indicated by the weaker intensity of the chemical shift at 71 ppm. Polar solvents can promote MIR,[45,46] but this faster MIR may increase the chance for the intramolecular MIC of ^{P}FpR before the occurrence of MIP *via* intermolecular reactions. By comparing the system in DMSO and DMF at 60 °C, the production of cyclic ^{P}FpR in the DMSO system is particularly favored. We attribute the difference to the solvent viscosity, as DMSO is twice more viscous than DMF. The high viscosity of DMSO (1.2 cP at 60 °C) may reduce the probability for intermolecular reactions and favor intramolecular MIC at the early stage of the reaction. Similarly, in DMF and THF, which are 2 and 4 times less viscous than DMSO, respectively, the formation of cyclic ^{P}FpR was reduced by a factor of 2 in DMF (Figure 3.13b), and 4 in THF (Figure 3.13c). If the hypothesis was right, intramolecular MIC can be suppressed by increasing the temperature to reduce solvent viscosity. As a result, solution MIP at a higher temperature (105 °C) in DMSO and DMF were attempted. As shown in Figure 3.13b, a higher temperature (105 °C) substantially reduced MIC in DMSO. Contradictorily, the reactions at 105 °C in DMF (Figure 3.13b) or in bulk (Figure 3.13d) did not suppress intramolecular MIC, but rather generated more ^{P}FpR ring complexes. The results of the reactions at a higher temperature (105 °C) can be understood as a result of the two effects: reduced viscosity and increased reaction rate at a higher temperature. The latter effect may be predominant in the DMF and bulk reaction systems resulting in a higher MIR rate and an increased probability for the production of cyclic ^{P}FpR at the early stage of the reaction. In terms of the reaction in bulk, the former effect may also increase the chance for intramolecular MIC for the production of cyclic

^{P}FpR. These results suggest that a polar solvent and a lower temperature (*ca.* 60 °C), which can suppress the rate of MIC, are ideal to favor (intermolecular) polymerization.

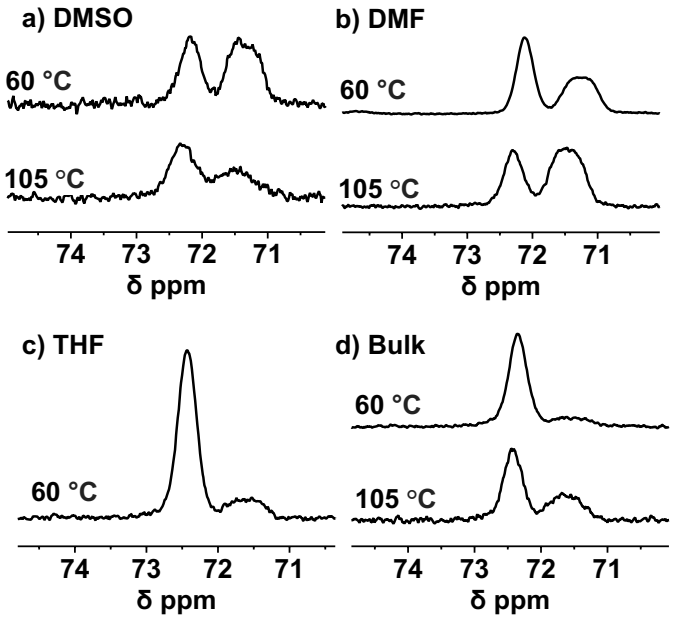

Figure 3.13: ^{31}P NMR spectra for crude products in $CDCl_3$ via MIP at 60 °C or 105 °C in a) 50 wt.% DMSO, b) 50 wt.% DMF, c) 50 wt.% THF, and d) 100 wt.% (or bulk).

3.3.2 Kinetic Study on Ring-closing MIP of ^{P}FpR

In order to better understand the nature of MIRs, a time-dependent kinetic study of MIP was performed. Samples were taken at various time intervals during MIP and monitored by ^{31}P NMR analysis. As shown in Figure 3.14, both intermolecular and intramolecular MIRs occur within the first hour, producing uncyclized P(^{P}FpR) oligomers and cyclized ^{P}FpR monomer, as indicated by the appearance of the chemical shifts at 72 ppm and 71 ppm (Fe-P bond), as well as a chemical shift at -15.6 ppm (PPh_2 end group of uncyclized oligomers). This result suggests that MIP and MIC are two competing reactions that both occur at the early stage of MIR. This result also explains the increased intensity of the chemical shift at 71 ppm when the temperature was increased from 60 °C to 105 °C in DMF (Figure 3.13b) and in bulk (Figure 3.13d), which generated

more intramolecular MIC products at the beginning, due to the increased rates of both completing reactions.

After 6 hours of MIP the monomer signal at -15.8 ppm disappeared, which is due to the complete conversion of ^{P}FpR monomer into uncyclized P(^{P}FpR) polymers (with phosphine end group) and cyclized ^{P}FpR monomer. However, the shift at -15.6 ppm remains, suggesting the presence of uncyclized P(^{P}FpR) oligomers with the phosphine end group. This shift representing the phosphine end group (-15.6 ppm) completely vanished after 24 hours, which indicates that all the oligomers were cyclized into P(^{P}FpR) macrocycles.

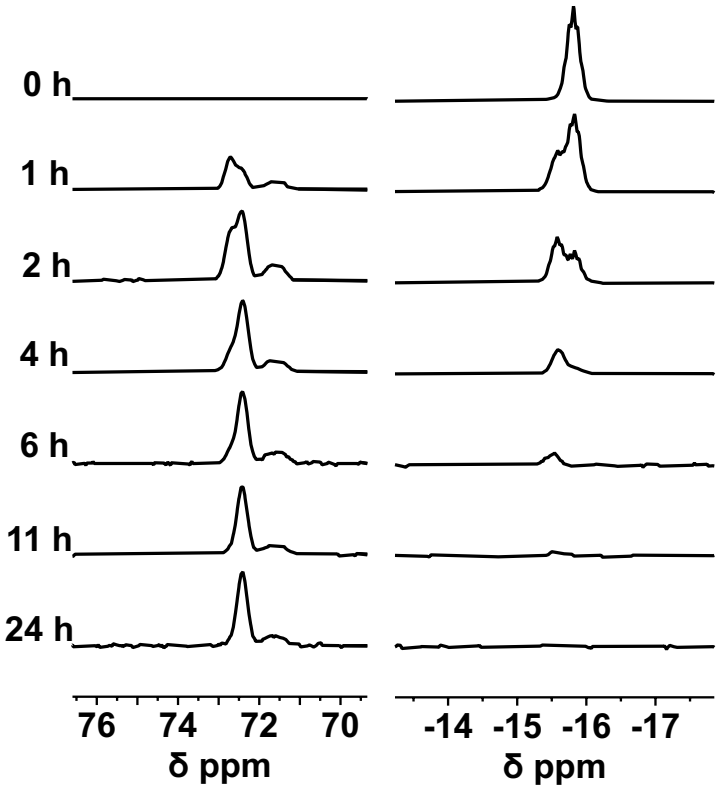

Figure 3.14: Time-dependent ^{31}P NMR ($CDCl_3$) spectra for the MIP of ^{P}FpR.

3.3.3 Concentration effect on MIP

It is well-known that a low concentration favors intramolecular cyclization.[18] The concentration effect on MIP was therefore investigated to vary the production of the cyclic

molecules, P(^{P}FpR) macrocycles and ^{P}FpR rings. Figure 3.15 illustrates the ^{31}P NMR spectra for the crude products resulting from the reactions in THF with various monomer concentrations at 60 °C. As shown in Figure 3.15, when the monomer concentration was low (1 wt.%), only one signal at 71 ppm was observed, indicating that only intramolecular MIC was taken place to produce Fe-P bonded ^{P}FpR rings, and no MIP occurred under such diluted conditions. By increasing the monomer concentration, the intensity of the signal at 71 ppm decreased, which suggests that MIC was suppressed by a higher concentration. For the systems with a concentration higher than 70 wt.%, MIC was significantly suppressed and the major product was the macrocycles produced by ring-closing MIP. The occurrence of the ring-closing process yielding P(^{P}FpR) macrocycles at high concentrations, and even in bulk, is attributed to the coordination geometry of the repeating units (non-linear, piano-stool geometry) and the low rotation barrier of the Fe-Cp bonds in the monomer,[43] which can form a cyclic conformation for the polymer backbone.

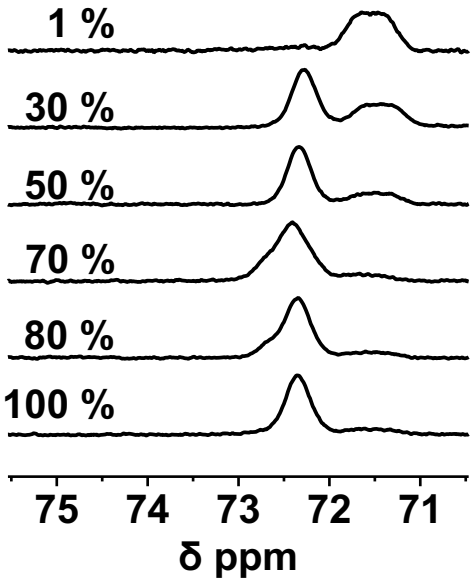

Figure 3.15: ^{31}P NMR spectra for the crude product prepared by MIP in THF at 1-100 wt.% monomer concentrations at 60 °C for 48 hours.

The GPC analysis results for the P(^{P}FpR) macrocycle, produced from the systems with the monomer concentrations greater than 50 wt.% are presented in Figure 3.16. The highest MW of P(^{P}FpR) macrocycles was obtained at 70 wt.%, with a M_p of 17,500 g/mol, corresponding to a DP of 36. The lower concentration (50 wt.%) resulted in a lower M_p of *ca.* 11,200 g/mol. These results are reasonable, as a lower concentration favors intramolecular MIC. By increasing the monomer concentration to 80 wt.% and 100 wt.% (bulk), however, the M_p reduced to 7,000-8,500 g/mol. As we observed that the reaction systems with a concentration above 70 wt.% became bulk-like, the smaller macrocycles produced are rationalized by reduced mobility of the oligomers having a cyclic conformation, and tending to undergo intramolecular cyclization.

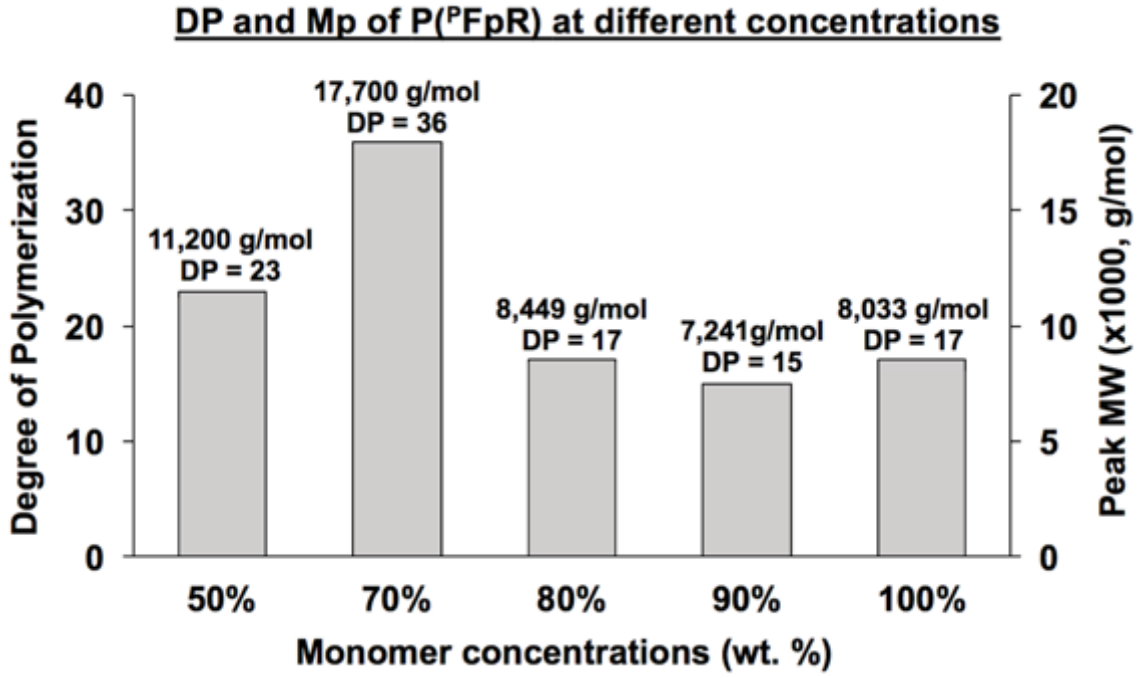

Figure 3.16: GPC data for P(^{P}FpR) macrocycles, R = $(CH_2)_4CH{=}CH_2$, at different concentrations. Monomer concentration (wt. %) in THF. Peak MW in g/mol, relatively to PS standards, determined by GPC analysis in DMF.

4.0 Conclusions

In summary, two synthetic routes for the effective synthesis of cyclic molecules were identified to produce exclusively cyclic ^{P}FpR monomer and P(^{P}FpR) macrocycles via migratory insertion reactions (MIRs) of ^{P}FpR (Figure 4.1). Cyclic formation is attributed to the non-linear, piano-stool geometry of the ^{P}FpR monomers, as well as the low rotation barrier of the Cp-Fe bond in the polymer backbone. The MIR conditions, including the temperature, solvent and monomer concentration were varied to examine their influences on the production of ring molecules. Two novel cyclic compounds, ^{P}FpR rings for R = $(CH_2)_5CH_3$ and $(CH_2)_4CH{=}CH_2$, were produced in high yield *via* intramolecular migratory insertion cyclization (MIC), which is favored at a low monomer concentration in polar solvents of high viscosity. Their chemical structures were confirmed and fully characterized by NMR spectroscopy, ESI-MS, FT-IR, and X-ray crystallography. On the other hand, the P(^{P}FpR) macrocycles, with M_p up to 17,500 g/mol, were obtained by ring-closing migration insertion polymerization (MIP), which is favored at a high monomer concentration (70 wt.%) in polar solvents with a low viscosity at low temperature (60 °C). The MW of P(^{P}FpR) macrocycles was also shown to be affected by the monomer concentration. Above 70 wt.%, the efficiency of step-growth cyclization was reduced due to the high viscosity of the system, producing lower MW P(^{P}FpR) macrocycles.

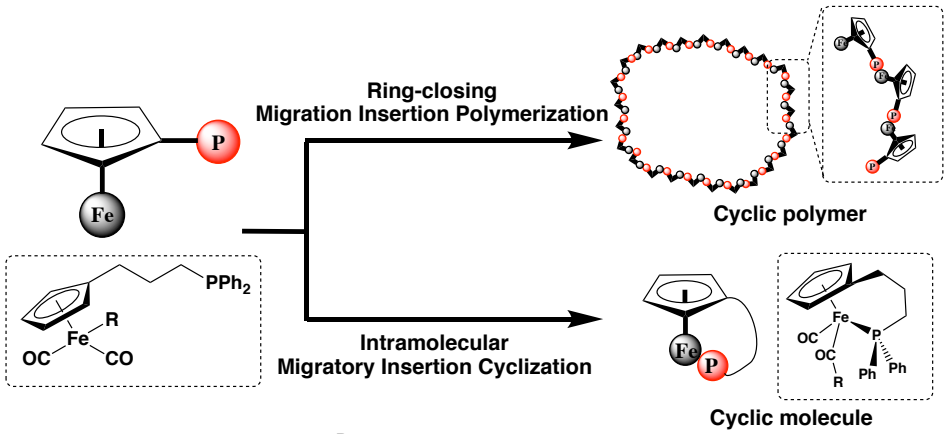

Figure 4.1: Summary of MIRs of ^{P}FpR.

5.0 Future Work

The successful synthesis of novel Cp-phosphane-bridged ^{P}FpR ring complexes, for R = $(CH_2)_5CH_3$ and $(CH_2)_4CH{=}CH_2$, *via* intramolecular MIC offers new opportunities to synthesize new derivatives with different R-groups, transition metal centers and/or carbon spacers. Investigations into the properties (*i.e.* redox properties due to the presence of iron) and applications of such complexes as functional materials can be promising for future research. For example, the self-assembly study of ^{P}Fp$(CH_2)_4CH{=}CH_2$ is being studied in our group, in which our preliminary results have shown interesting self-assembly behavior in (5:5 v/v) THF/water system. The effect of cyclized molecules in self-assembly can be further investigated, by comparing the self-assembly behaviors of uncyclized ^{P}FpR and cyclized ^{P}FpR rings. In addition, the P(^{P}FpR) macrocycles, for R = $(CH_2)_4CH{=}CH_2$, can be post-modified by click reactions, such as hydrosilylation and thiol-ene reactions, to form larger size grafted copolymers. The carbonyl groups in the polymer backbone may allow host-guest interactions, which could be used in drug delivery systems.

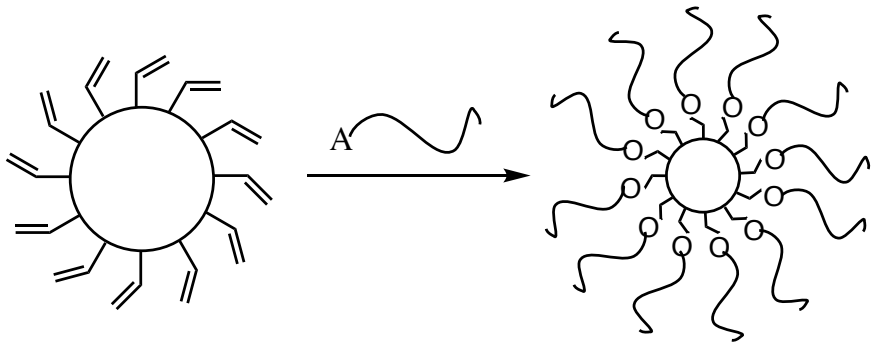

Scheme 5.1: Post-polymerization modification of P(^{P}FpR) macrocycles by click reactions.

References

[1] I. Manners, *Adv. Organomet. Chem*., **199**5, 37, 131-168.

[2] H. Butenchon, *Chem. Rev*., **2000**, 100, 1527-1564.

[3] M. Ogasawara, Y. Tseng, S. Arae, T. Morita, T. Nakaya, W. Wu, T. Takahashi and K. Kamikawa, *J. Am. Chem. Soc*., **2014**, 136, 9377-9384.

[4] K. Kamikawa, Y. Tseng, J. Jian, T. Takahashi and M. Ogasawara, *J. Am. Chem. Soc*., **2017**, 139, 1545-1553.

[5] I. Manners, *Polyhedron*, **1996**, 15, 4311-4329.

[6] D. E. Herbert, U. F. J. Mayer and I. Manners, *Angew. Che, Int. Ed*., **2007**, 46, 5060-5081.

[7] F.A. Cotton, *Helv. Chim. Acta*, **1967**, 50, 117-130.

[8] R. Xu, W. Pang and Q. Huo, *Modern Inorganic Synthetic Chemistry*, Elsevier: Oxford, **2001**.

[9] K. H. Pannell and H. K. Sharma, *Organometallics*, **2010**, 29, 4741-4745.

[10] H. K. Sharma, F. Cervantes-Lee and K. H. Pannell, *J. Am. Chem. Soc*., **2004**, 126, 1326-1327.

[11] A. C. McConnell, P. J. Pogorzelec, A. M. Z. Slawin, G. L. Williams, P. I. P. Elliott, A. Haynes, A. C. Marr and D. J. Cole-Hamilton, *Dalton Trans*., **2006**, 91-107.

[12] J. Foerstner, R. Kettenbach, R. Goddard and H. Butenschon, *Chem. Ber*. **1996**, 129, 319-325.

[13] A. Dohring, V. R. Jensen, P. W. Jolly, W. Thiel and J. C. Weber, *Organometallics*, **2001**, 20, 2234-2245.

[14] K. Kunz, G. Erker, S. Doring, R. Frohlich and G. Kehr, *J. Am. Chem. Soc.,* **2001**, 123, 6181-6182.

[15] S. Kosher and H. Butenschon, *Eur. J. Inorg. Chem*., **2018**, 31-45.

[16] G. Wang, J. Yin, J. Li, Z. Yin, W. Zhang and Z. Xi, *Inorg. Chem. Front*., **2019**, 6, 428-433.

[17] Y. Zhu and N. S. Hosmane, *ChemistryOpen*, **2015**, 4, 408-417.

[18] T. Josse, J. De Winter, P. Gerbaux and O. Coulembier, *Angew. Chem. Int. Ed*., **2016**, 55, 13944-13958.

[19] X. Tu, M. Liu and H. Wei, *J. Polym. Sci. Part A*, **2016**, 54, 1447-1458.

[20] D. Freifelder, A. K. Kleinschmidt and R. L. Sinsheimer, *Science*, **1964**, 146, 254–255

[21] R. J. Williams, A. P. Dove and R. K. O'Reilly*, Polym. Chem*., **2015**, 6, 2998-3008.

[22] J. W. Steed, Coord. *Chem. Rev*., **2001**, 215, 171-221.

[23] M. V. Rekharsky and Y. Inoue, *Chem. Rev*., **1998**, 98, 1875-1917.

[24] R. Challa, A. Ahuja, J. Ali, and R. K. Khar, *AAPS PharmSciTech*, **2005**, 6, E329-E357.

[25] B. Gidwani and A. Vyas, *Biomed Res. Int*., **2015**, 1-15.

[26] K. Zhang and G. N. Tew, *ACS Macro Lett*., **2012**, 1, 574-579.

[27] C. W. Bielawski, D. Benitez, R. H. Grubbs*, J. Am. Chem. Soc*., **2003**, 125, 8424-8425.

[28] M. Kubo, T. Hayashi, H. Kobayashi, K. Tsuboi, T. Itoh, *Macromolecules*, **1997**, 30, 2805-2807.

[29]: F. S. Arimoto and A. C. Haven*, J. Am. Chem. Soc*., **1955**, 77, 6295-6297.

[30]: K. A. Williams, A. J. Boydston, and C. W. Bielawski, *Chem. Soc. Rev*. **2007**, 36, 729-744.

[31] M.S. Inkpen, S. Scheerer, M. Linseis, A. J. P. White, R. F. Winter, T. Albrecht and T. J. Long, *Nature Chemistry*, **2016**, 8, 825-830.

[32] D. E. Herbert, J. B. Gilroy, W. Y. Chan, L. Chabanne, A. Staubitz, A. J. Lough and I. Manners., *J. Am. Chem. Soc*., **2009**, 131, 14958-14968.

[33] J. Chen, H. Li, H. Zhang, X. Liao, H. Han, L. Zhang, R. Sun and M. Xie, *Nature Communication*, **2018**, 9, 1-9.

[34] S. N. Magonov and D. H. Reneker, *Annu. Rev. Mater. Sci.*, **1997**, 27, 175-222.

[35] M. Schappacher and A. Deffieux, *Science*, **2008**, 319, 1512-1515.

[36] A. J. Boydston, T. W. Holcombe, D. A. Unruh, J. M. Frechet and R. H. Grubbs, *J. Am. Chem. Soc*., **2009**, 131, 5388-5389.

[37] Y. Xia, A. J. Boydston and R. H. Grubbs, *Angew. Chem. Int. Ed.*, **2011**, 50, 5882-5885.

[38] K. Zhang, M. A. Lackey, Y. Wu and G. N. Tew, *J. Am. Chem. Soc*., **2011**, 133, 6906-6909.

[39] M. Green and D. J. Westlake, *J. Chem. Soc. A*, **1971**, 367-371.

[40] X. Wang, K. Cao, Y. Liu, B. Tsang, and S. Liew, *J. Am. Chem. Soc*., **2013**, 135, 3399-3402.

[41] K. Cao, B. Tsang, Y. Liu, D. Chelladural, W. P. Power, and X. Wang, *Organometallics*, **2014**, 33, 531-539.

[42] J. Liu, Z. Guan, X. Tian, J. Lin, and X. Wang, *Polym. Chem*., **2016**, 7, 4419-4426.

[43] K. Cao, L. Peng, J. Zhu, A. Feng, D. Liu, A. Worku, S. Liu, J. Lin, J. Yuan, X. Wang, *Chem. Eur. J.*, **2018**, 24, 15380-15386.

[44] P. R. Andres and U. S. Schubert, *Macromol. Rapid Commun,.* **2004**, 25, 1371-1375.

[45] K. Nicholas, S. Rachu and M. Rosenblum, *J. Organomet. Chem.*, **1974**, 78, 133-137.

[46] K. Cao, J. Ward, R. C. Amos, M. G. Jeong, K. T. Kim, M. Gautiher, D. Foucher and X. Wang, *Chem. Commun.*, **2014**, 50, 10062-10065.

Appendix

A1. NMR characterization of ^{P}FpR ring, for R = $(CH_2)_5CH_3$

The ^{P}FpR with a hexyl chain was also characterized in the same manner as the characterization discussed in section 3.2.2. In the corresponding ^{1}H NMR spectrum (Figure A1a), the protons (a-d, Cp, and Ph) were assigned based on the previous proton assignments with R = $(CH_2)_4CH=CH_2$ (Figure A1b), which shows consistent chemical shifts and signal patterns. The chemical shifts at 7.6-7.2 ppm were assigned to the 10 Ph protons, and the chemical shifts at 4.7-3.9 were assigned to the 4 Cp protons. The diastereotopic protons (b-d) were assigned to the chemical shifts at 2.17 ppm and 1.40 ppm, 2.78 ppm and 2.40 ppm, and 2.54 ppm and 1.99 ppm for H_b, H_c, and H_d, respectively. H_a was assigned to the chemical shift at 2.54 ppm. The chemical shift at 0.79 ppm was assigned to the protons (H_f) on the hexyl chain end (CH_3). The chemical shifts from 2.17-0.86 ppm were assigned to the rest of the protons (H_e) on the hexyl chain. Similarly, the ^{13}C NMR spectrum (Figure A2) also showed consistent peaks patterns for R = $(CH_2)_4CH=CH_2$. The chemical shifts at 279 ppm and 220 ppm were assigned to the acyl carbon and the terminal CO carbon, respectively. The Ph carbons and Cp carbons were assigned to the chemical shifts at 138-128 ppm and 99-73 ppm, respectively. The chemical shift at 65.8 ppm was assigned to the carbon adjacent to the acry CO group. The CH_3 carbon was assigned to 14 ppm. COSY (Figure A3) and HMQC (Figure A4) 2D NMR were also attempted to solve the peak assignments for the carbons and protons on the hexyl chain, but their overlapping peaks made it difficult to assign each chemical shift accurately.

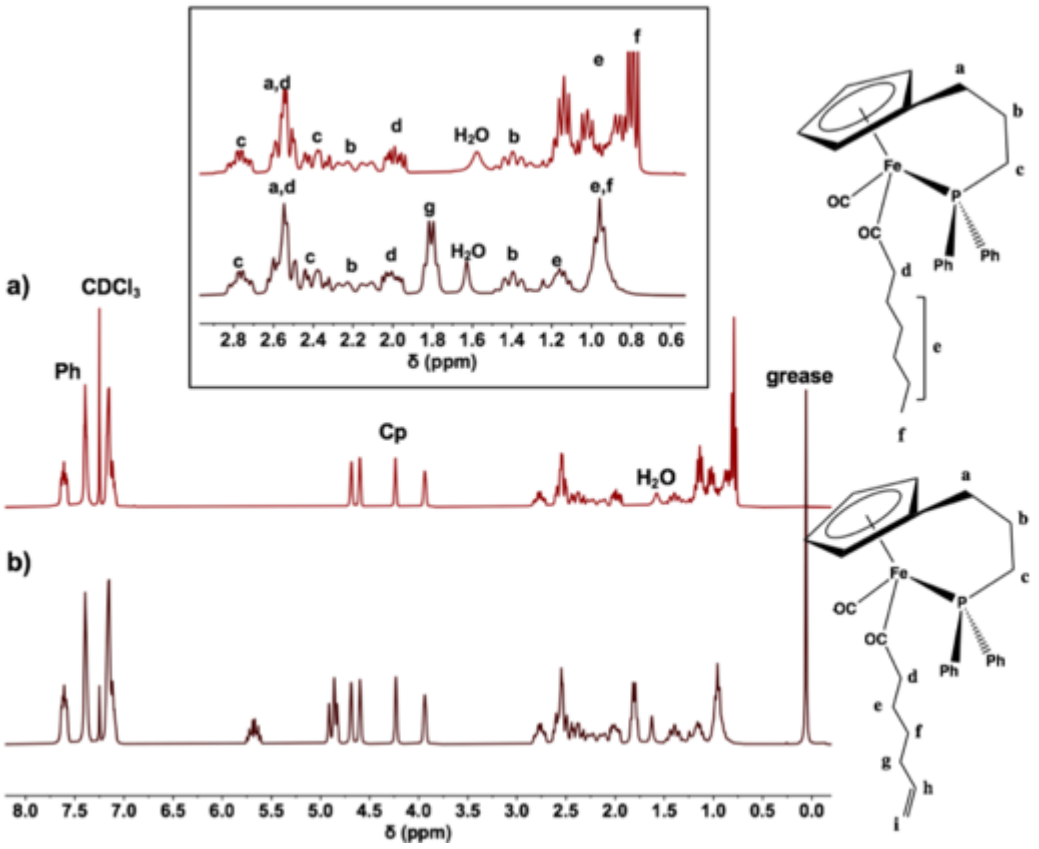

Figure A1: ^{1}H NMR ($CDCl_3$) spectra for cyclic ^{P}FpR, for R = a) $(CH_2)_5CH_3$ and b) $(CH_2)_4CH{=}CH_2$.

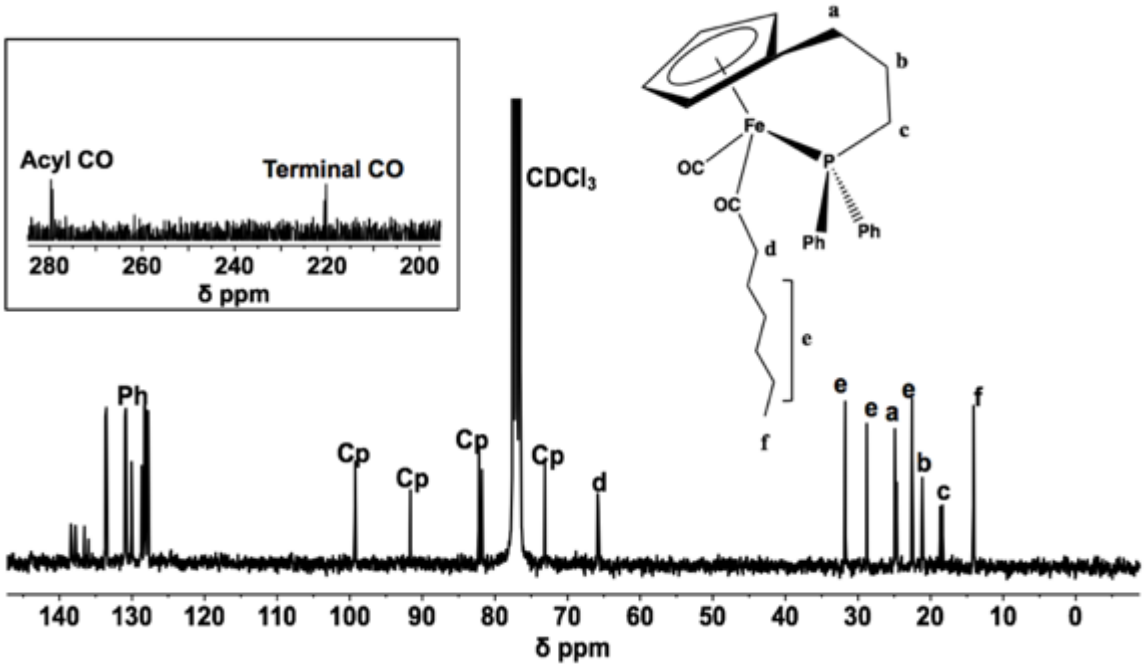

Figure A2: ^{13}C NMR ($CDCl_3$) spectra for cyclic ^{P}FpR, for R = $(CH_2)_5CH_3$

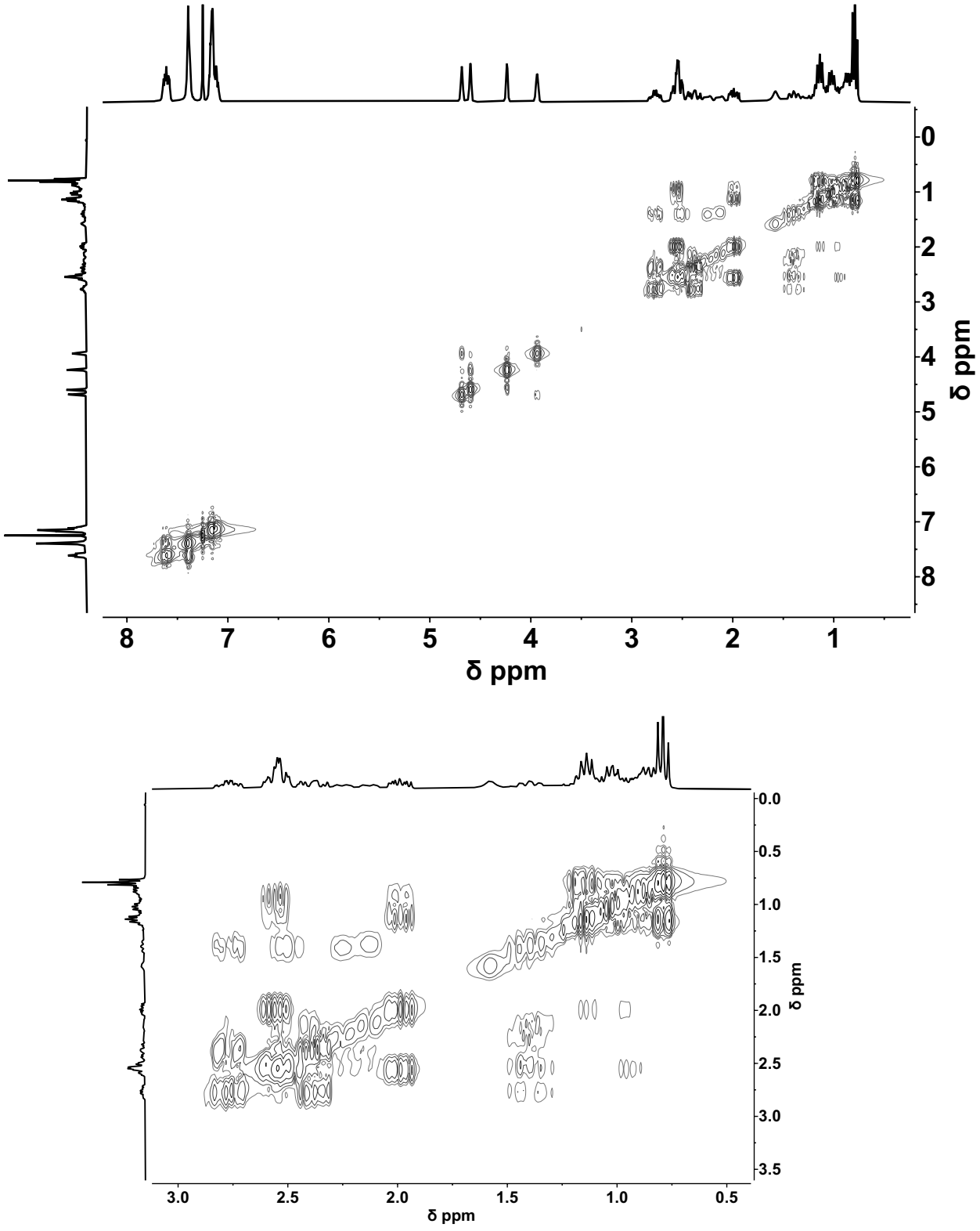

Figure A3: COSY NMR ($CDCl_3$) spectra for cyclic ^{P}FpR, for R = $(CH_2)_5CH_3$

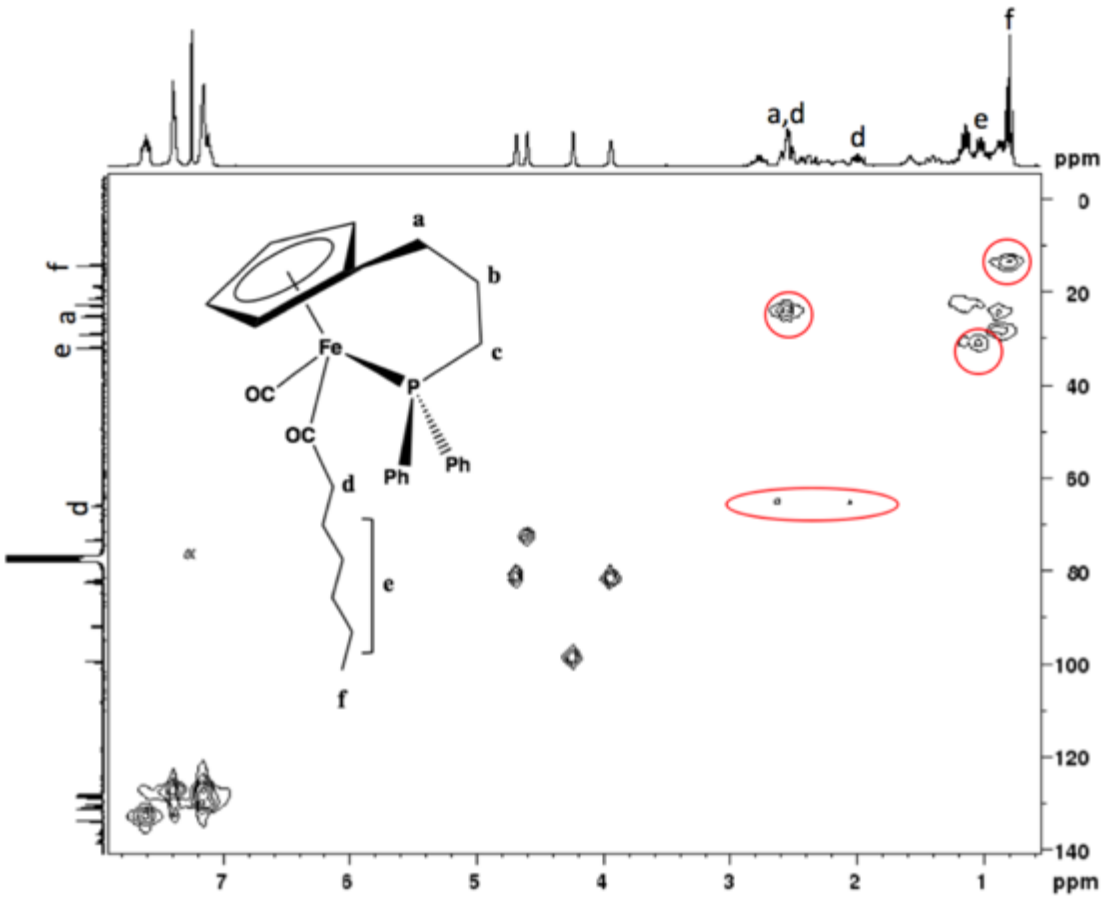

Figure A4: HMQC NMR ($CDCl_3$) spectra for cyclic ^{P}FpR, for R = $(CH_2)_5CH_3$.